ORIGINAL PAPER

A mesh-independent finite element formulation for modeling crack growth in saturated porous media based on an enriched-FEM technique

A. R. Khoei · M. Vahab · E. Haghighat ·
S. Moallemi

Abstract In this paper, the crack growth simulation is presented in saturated porous media using the extended finite element method. The mass balance equation of fluid phase and the momentum balance of bulk and fluid phases are employed to obtain the fully coupled set of equations in the framework of $u-p$ formulation. The fluid flow within the fracture is modeled using the Darcy law, in which the fracture permeability is assumed according to the well-known cubic law. The spatial discritization is performed using the extended finite element method, the time domain discritization is performed based on the generalized Newmark scheme, and the non-linear system of equations is solved using the Newton–Raphson iterative procedure. In the context of the X-FEM, the discontinuity in the displacement field is modeled by enhancing the standard piecewise polynomial basis with the Heaviside and crack-tip asymptotic functions, and the discontinuity in the fluid flow normal to the fracture is modeled by enhancing the pressure approximation field with the modified level-set function, which is commonly used for weak discontinuities. Two alternative computational algorithms are employed to compute the interfacial forces due to fluid pressure exerted on the fracture faces based on a 'partitioned solution algorithm' and a 'time-dependent constant pressure algorithm' that are mostly applicable to impermeable media, and the results are compared with the coupling X-FEM model. Finally, several benchmark problems are solved numerically to illustrate the performance of the X-FEM method for hydraulic fracture propagation in saturated porous media.

1 Introduction

Materials such as soil and concrete possess considerable amount of voids that significantly affect the mechanical behavior of porous materials. In such materials, two behaviors can be distinguished; one is due to the solid skeleton which acts as the primary load transmitter constituent and the other is fluid phase acting as filler for voids with its special effects. The mechanical behavior of the fully or partially saturated porous medium and in particular of soils, is governed largely by the interaction of the solid skeleton with the pore fluid, generally water, present in the pore structure. The interaction between the solid and fluid phases leads to a complicated coupled behavior in the porous media. Generally, porous media are described as multiphase media with separate velocities and stresses for each phase, thereby the stress acting on the solid skeleton is usually referred to as effective stress, and the hydro-

A. R. Khoei (✉) · M. Vahab · E. Haghighat · S. Moallemi
Department of Civil Engineering, Center of Excellence in Structures and Earthquake Engineering, Sharif University of Technology, P.O. Box 11365-9313, Tehran, Iran
e-mail: arkhoei@sharif.edu

static stress acting on the fluid phase is denoted as the excess pore fluid pressure.

The first study on deformable porous media was presented by Terzaghi (1943) in one dimensional consolidation of soil column. Biot (1941) and Biot and Willis (1957) developed a complete expression for governing equations of two phase saturated porous media. The mixture theories were developed by Green and Naghdi (1969); the volume fractions were introduced by Morland (1972) and Bowen (1976); and an alternative derivation of Biot coupled equations were presented by Ghaboussi and Wilson (1972) and Derski (1978). Rice and Cleary (1976) applied the Biot linearized quasistatic elasticity theory of fluid-infiltrated porous materials to solve the introduced edge dislocation with concentrated line force and the pressurized cylindrical and spherical cavity. A plasticity theory of saturated porous media was presented by Boer and Kowalski (1983), and a more common formulation for non-linear analysis of deformable porous media was proposed by Zienkiewicz and Shiomi (1984). An explicit computation algorithm was presented by Zienkiewicz et al. (1990a,b) for modeling the static and dynamic behavior of deformable porous media. Simoni and Schrefler (1991) developed a formulation for flow of water and oil through porous media, and Schrefler and Zhan (1993) modified the formulation by considering the effects of air flow. In addition, there are several recently mathematical models proposed in the literature for fully and partially saturated porous materials (Schrefler et al. 1995; Lewis and Rahman 1999). These models are generally on the basis of typical simplifying assumptions, such as the rigid soil skeleton with no solid deformation (Wu and Forsyth 2001), the static gas phase with null gas flow and uniform gas pressure equal to the atmospheric pressure (Sheng et al. 2003), the omission of phase transitions (Schrefler and Scotta 2001; Oettl et al. 2004), and the quasi-static condition (Stelzer and Hofstetter 2005). A detailed literature review on porous media can be found in Lewis and Schrefler (1998), Zienkiewicz et al. (1999) and Coussy (2004).

The finite element method has been successfully employed for numerical simulation of differential equations in various engineering problems. Despite the capability of FEM technique in the solution of continuum mechanics problems, there are some difficulties in modeling of discontinuities such as fracture mechanics problems with the standard FEM method. In fact, in the approaches based on the standard FEM, modeling of crack growth is restricted to the inter-element boundaries, suffering from the problem of mesh dependency, or successive remeshing is carried out to overcome the sensitivity to the mesh generated and avoid the preferred directions when the crack is propagating (Khoei et al. 2008b, 2009; Moslemi and Khoei 2009), which makes the crack growth simulation a computationally expensive and cumbersome process. Various methods have been developed for modeling such phenomenon, among them the extended finite element method is a powerful technique that benefits from the concept of standard FEM method by employing the enrichment shape functions based on the partition of unity property. In this manner, the difficulties confronted in the standard FEM are handled by locally enriching the conventional finite element approximation with an additional function through the concept of the partition of unity, which was introduced in the pioneering work of Melenk and Babuska (1996). This idea was then exploited to set up the framework of extended finite element method by Belytschko and Black (1999) and Moës et al. (1999). Indeed, the extended finite element approximation relies on the partition of unity property of finite element shape functions for the incorporation of local enrichments into the classical finite element basis. By appropriately selecting the enrichment function and enriching specific nodal points through the addition of extra degrees of freedom relevant to the chosen enrichment function to these nodes, the enriched approximation would be capable of directly capturing the local property in the solution (Daux et al. 2000; Sukumar et al. 2001; Belytschko et al. 2001). Based on the X-FEM, the evolving crack is simulated independently of the underlying finite element mesh and without continuous remeshing of the domain as the crack grows. Since the finite element mesh does not need to conform to the crack geometry, and thus the need for the costly mesh regeneration and data transfer between two successive meshes is eliminated, the X-FEM facilitates the modeling of the propagating crack. The technique has been applied in crack problems, including: the crack growth with frictional contact by Dolbow et al. (2001), cohesive crack propagation by Moës and Belytschko (2002), fatigue crack growth by Stolarska and Chopp (2003), stationary and growing cracks by Ventura et al. (2003), three-dimensional crack propagation by Areias and Belytschko (2005), and dynamic crack propagation by Remmers et al. (2008). A review on the extended finite element method was presented

by Belytschko et al. (2009) and Fries and Belytschko (2010). The application of X-FEM for modeling of fluid flow in porous media has drawn considerable attention by researchers. In this regard, the shear band evolution in fluid saturated porous media was modeled by Réthoré et al. (2007a), the fluid flow in fractured saturated systems was treated by Réthoré et al. (2007b), the strong discontinuities in partially saturated porous media was proposed by Callari et al. (2010), the saturated porous media with material interfaces was modeled by Khoei and Haghighat (2011), and recently the hydro-mechanical modeling of cohesive crack propagation in multiphase porous media was performed by Mohammadnejad and Khoei (2013a,b).

In the present study, the extended finite element method that was recently developed by Mohammadnejad and Khoei (2013b) for cohesive crack propagation in multiphase porous media, was extended to model the dynamic mixed-mode crack propagation in saturated porous media. The mass balance equation of fluid phase is applied together with the momentum balance of bulk and fluid phases to obtain the fully coupled set of equations in the framework of $u-p$ formulation. The fluid flow within the fracture is modeled using the Darcy law, in which the fracture permeability is assumed according to the well-known cubic law. The spatial domain discritization is performed based on the X-FEM method, and the time domain discritization is carried out using the generalized Newmark scheme. In order to incorporate the fracture opening and the fluid exchange between the fracture and the surrounding porous medium, several modifications are applied into the X-FEM formulation. In this regard, the displacement jump requires that the displacement field be discontinuous across the fracture. In addition, the fluid exchange implies that the fluid flow, which is governed by the Darcy velocity of the fluid, in the normal direction to the fracture be discontinuous. Since the Darcy velocity is related to the fluid pressure gradient by means of the Darcy law, the normal gradient of the fluid pressure must be discontinuous across the fracture. In the context of the X-FEM, the discontinuity in the displacement field is modeled by enhancing the standard piecewise polynomial basis with a discontinuous enrichment function; and the discontinuity in the fluid flow normal to the fracture is modeled by enhancing the standard finite element approximation of the pressure field with the commonly used enrichment function for weak discontinuities. For the numerical solution, the unconditionally stable direct time-stepping procedure is applied to resolve the resulting system of strongly coupled nonlinear algebraic equations using the Newton–Raphson iterative algorithm. As a result, the solid displacement and fluid pressure fields are obtained simultaneously together with the fracture length. Furthermore, the fluid leak-off is obtained as a part of the solution process without introducing any simplifying assumption. Finally, several numerical examples are presented to demonstrate the capability and the efficiency of the developed model in the fully coupled simulation of hydraulically driven fractures in deformable porous media. It is noteworthy to highlight that the current study is an extension of a recently published paper by Mohammadnejad and Khoei (2013b) developed to model the dynamic mixed-mode crack propagation of saturated porous media with a special reference to the hydraulically driven fracture propagation in a concrete gravity dam, in which two alternative computational algorithms are employed to compute the interfacial forces due to fluid pressure exerted on the fracture faces based on a 'partitioned solution algorithm' and a 'time-dependent constant pressure algorithm' that are mostly applicable to impermeable media.

2 Governing equations of deformable porous media with discontinuity

Porous medium refers to material that consists of solid grains known as the solid skeleton and at least one fluid phase such as water or gas that flows through solid grains. Modeling of the hydraulic fracture propagating in the porous medium involves the coupling of various physical phenomena, including the deformation of the solid skeleton, the pore fluid flow through the porous medium surrounding the fracture, the fluid flow within the fracture, the fluid exchange between the fracture and the surrounding porous medium, and the propagation of the hydraulic fracture. The partial differential equations governing the hydraulic fracture propagation in the porous medium consist of the equilibrium equation for the whole mixture and the continuity equation for the fluid flow inside the fracture and through the surrounding porous medium. The Darcy law with the constant intrinsic permeability is assumed to hold for the pore fluid flow in the porous medium surrounding the fracture. Assuming that the flow of the fracturing fluid

within the fracture is steady, the Darcy law is valid for the fluid flow within the fracture. However, in contrast to the porous medium, the intrinsic permeability within the fracture cannot be assumed to be constant. Thus, the Poiseuille or cubic law is employed to define the intrinsic permeability within the fracture. The validity of the cubic law has been shown in the case of the laminar flow of the Newtonian viscous fluid through fractures with smooth, parallel walls (Witherspoon et al. 1980). The deviation from the ideal parallel faces conditions causes an apparent decrease in the fluid flow through the fracture. This effect can be taken into account by incorporating a coefficient into the cubic law. In fact, this coefficient considers the influence of the fracture roughness and the fracture opening variation on the fluid flow.

Basically, two strategies have been used to describe the porous media as a continuum body, one is the mixture theory integrated by the concept of volume fractions, and the other is the averaging theory that describes the porous media from a micro-mechanical point of view. In this study, the mixture theory of porous media based on the Biot theory is employed to describe the behavior of deformable porous media. One of the most important concepts in the mixture theory is the degree of saturation for non-solid phases, which is defined by the ratio of volume of the phase to the total volume of pores. In a fully saturated porous media with only one pore fluid, the degree of saturation of non-solid phase is defined as $S_w = 1$. In addition, the density of total mixture can be defined for the soil-fluid domain as $\rho = n\rho_w + (1-n)\rho_s$, where ρ_w is the density of fluid phase and ρ_s is the density of solid grains. The total stress tensor can be defined as $\boldsymbol{\sigma} = \boldsymbol{\sigma}' - \alpha p\mathbf{I}$, with $\boldsymbol{\sigma}'$ denoting the effective stress acting between solid grains, and p is an average pressure of fluid phases. Parameter α is a corrective coefficient of pore pressure effect on solid grains, in which for isotropic materials can be computed by $\alpha = 1 - K_T/K_S$, where K_T and K_S are the bulk modulus of soil sample and solid grains, respectively, and for most soils are given as $\alpha \approx 1$.

2.1 Mathematical model of saturated porous media

In order to derive the governing equations of porous media, the Biot theory is employed in an updated Lagrangian framework (Khoei et al. 2004). Consider a two-phase media, in which the fluid phase is par-

tially saturated under the condition of $p_g = 0$, and the convective terms are neglected. The motion of total mixture is defined by the motion of solid-fluid mixture $u_i(\boldsymbol{x}, t)$ and the relative motion of fluid with respect to the mixture $w_i(\boldsymbol{x}, t)$. The governing equations are the total solid-fluid mixture, the linear momentum-balance and the continuity equation for each phase. The linear momentum-balance of solid-fluid mixture can be written by neglecting the relative acceleration of fluid phase with respect to the solid phase, i.e. $\ddot{w}_i \approx 0$, as

$$\nabla \cdot \boldsymbol{\sigma} - \rho\ddot{\mathbf{u}} + \rho\mathbf{b} = 0 \qquad (1)$$

where $\ddot{\mathbf{u}}$ is the acceleration vector of the solid phase, $\mathbf{b}$ is the body force vector, ρ is the average density of the whole mixture, and the symbol ∇ denotes the vector gradient operator.

The conservation of linear momentum for the fluid flow results in the generalized Darcy equation. Assuming negligibility of the relative acceleration term of the fluid, the momentum-balance of the fluid phase, or the Darcy relation for the pore fluid flow through the porous medium surrounding the fracture can be written as

$$-\nabla p - \mathbf{R} - \rho_f\ddot{\mathbf{u}} + \rho_f\mathbf{b} = 0 \qquad (2)$$

where $\mathbf{R}$ denotes the viscous drag force defined by the Darcy seepage law as $\dot{\mathbf{w}} = \boldsymbol{k}_f\mathbf{R}$, with $\boldsymbol{k}_f$ denotes the permeability matrix of the porous medium with respect to the pore fluid in which its dimension is defined as $(\text{length})^3(\text{time})/(\text{mass})$.

Finally, the continuity equation of fluid phase can be written as

$$\nabla \cdot \dot{\mathbf{w}} + \alpha\nabla \cdot \dot{\mathbf{u}} + \frac{1}{Q}\dot{p} = 0 \qquad (3)$$

where $1/Q \equiv (\alpha - n)/K_s + n/K_f$, in which K_s and K_f are the bulk moduli of the solid and fluid phases, respectively. Equations (1), (2) and (3) are the coupled governing equations of porous saturated media with variable set (u_i, w_i, p). Performing some mathematical manipulations, the set of equations can be modified as $u - p$ formulation of porous media which is appropriate to model the saturated porous material, which is much more appropriate for loading conditions up to earthquake frequencies (Zienkiewicz et al. 1999). Combining Eqs. (2) and (3) results in

$$\nabla \cdot \left[\boldsymbol{k}_f\left(-\nabla p - \rho_f\ddot{\mathbf{u}} + \rho_f\mathbf{b}\right)\right] + \alpha\nabla \cdot \dot{\mathbf{u}} + \frac{1}{Q}\dot{p} = 0 \quad (4)$$

It must be noted that in the above equation, it is common to neglect the contribution of solid acceleration to preserve the symmetry of final system of equations (Leung

Fig. 1 The boundary conditions of a fractured body Ω with a geomechanical discontinuity Γ_d
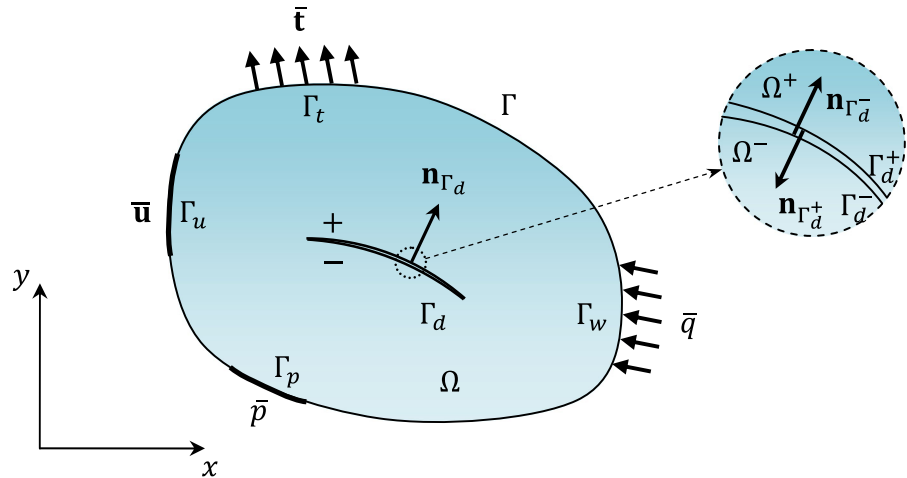
1984). It was shown in the literature that the effect of this term is not significant for the case of lower frequencies (Rice and Cleary 1976; Chan 1988; Coussy 2004; Detournay 2004), and can be excluded from the above equation (Zienkiewicz et al. 1999; Lewis and Schrefler 1998). Equations (1) and (4) are complemented by appropriate kinematical relation and the stress–strain constitutive equation. The kinematic equation is defined by the incremental strain–displacement relationship, and the stress–strain constitutive equation is defined by $d\boldsymbol{\sigma}' = \mathbf{D}\,d\boldsymbol{\varepsilon}$, with $\mathbf{D}$ denoting the forth order tangential stiffness matrix computed using an appropriate constitutive law.

The governing Eqs. (1) and (4) can be solved using the essential and natural boundary conditions. The solid-phase boundary conditions are $\mathbf{u} = \bar{\mathbf{u}}$ on Γ_u and $\mathbf{t} = \boldsymbol{\sigma} \cdot \mathbf{n}_\Gamma \equiv \bar{\mathbf{t}}$ on Γ_t with $\mathbf{n}_\Gamma$ denoting the unit outward normal vector to the external boundary Γ, in which $\Gamma = \Gamma_t \cup \Gamma_u$ is the boundary of domain. The fluid-phase boundary conditions are $\mathbf{p} = \bar{\mathbf{p}}$ on Γ_p and $\dot{\mathbf{w}} \cdot \mathbf{n}_\Gamma = \bar{q}$ on Γ_w which is the prescribed outflow rate of the fluid imposed on Γ_w with $\Gamma = \Gamma_p \cup \Gamma_w$, as shown in Fig. 1. From the physics of the problem, the existence of a discontinuity Γ_d in the porous medium leads to the mechanical and mass transfer couplings between the fracture and the porous medium surrounding the fracture. The mechanical coupling arises from the fluid pressure exerted on the fracture faces by injecting a viscous fluid into the fracture. The mass transfer coupling emanates from the fluid exchange between the fracture and the surrounding permeable porous medium. Hence, the essential and natural boundary conditions, which

hold on the complementary parts of the external boundary of the body, complete with the following boundary conditions on the discontinuity as $\boldsymbol{\sigma} \cdot \mathbf{n}_{\Gamma_d} = -p\mathbf{n}_{\Gamma_d}$ and $[\![\dot{\mathbf{w}}]\!] \cdot \mathbf{n}_{\Gamma_d} = \bar{q}_d$ on Γ_d, where $\bar{q}_d$ is the leakage flux of the fluid along the fracture toward the surrounding porous medium, which implies that there exists a discontinuity in the normal fluid flow across Γ_d, and $\mathbf{n}_{\Gamma_d}$ is the unit normal vector to the discontinuity Γ_d pointing to Ω^+ with $\mathbf{n}_{\Gamma_d} = \mathbf{n}_{\Gamma_d-} = -\mathbf{n}_{\Gamma_d+}$, as shown in Fig. 1. The notation $[\![\varXi]\!] = \varXi^+ - \varXi^-$ represents the difference between the corresponding values at the two crack faces. It is considered that the fluid pressure has the same value at both faces of the crack and pressure continuity from the crack faces to the surrounding porous medium holds along the crack boundary.

2.2 Mechanical behavior of fractured media

A convenient model to describe the mechanical behavior of fracture in quasi-brittle materials is based on the cohesive fracture model, originally introduced by Dugdale (1960) and Barenblatt (1962) and has since been used by many researchers to describe the near–tip nonlinear zone for cracks. Generally, the fracture process zone is a nonlinear zone characterized by progressive softening, where the traction across the forming crack surface decreases as separation increases. It was shown that the fracture process of concrete can be characterized by the strain softening and fracture toughening due to the formation and branching of micro-cracks (Shum and Hutchinson 1990; Jenq and Shah 1991). During the

fracture process, the high-stress state near the crack-tip causes micro-cracking at flaw sites, such as pores and air voids. This micro-cracking phenomenon consumes a part of the external energy introduced by the applied load, and the resulting micro-cracks can be produced with respect to the main crack plane. Generally, the crack surface is a tortuous path due to toughening mechanism, in which the crack generally branch around aggregates, causing random propagation in material. During the opening of a tortuous crack there may be some frictional sliding between the cracked faces that causes energy dissipation. The crack bridging and crack blunting may occur due to aggregates and air voids in the pathway of the main crack (Bazant and Planas 1998). The width and micro-cracking density distribution at the fracture front may vary depending on the structure size, shape, and type of loading. Owing to the stiffer matrix compared to fractures, most deformation in process zone occurs in the fractures, in the form of normal and shear displacement. As a result, the existing fractures may open, grow, or even induce new ones.

In order to model the fluid flow through the discontinuity, the continuity equation for the fluid flow within the fracture can be written according to Eq. (3) as

$$\nabla \cdot \dot{\mathbf{w}} + \alpha \nabla \cdot \dot{\mathbf{u}} + \frac{1}{K_f} \dot{p} = 0 \qquad (5)$$

where $\dot{\mathbf{w}}$ is the Darcy velocity vector of the fracturing fluid and is in fact the relative velocity of the fracturing fluid with respect to the solid phase defined as $\dot{\mathbf{w}} = k_{f_d} \left(-\nabla p - \rho_f \ddot{\mathbf{u}} + \rho_f \mathbf{b} \right)$, with k_{f_d} denoting the fracture permeability with respect to the fracturing fluid. For a viscous fluid flow with Newtonian rheology, the fracture permeability is estimated using the cubic law as

$$k_{f_d} = \frac{1}{\kappa} \frac{w^2}{12\mu_f} \qquad (6)$$

where $w = 2h$ is the fracture opening, μ_f denotes the dynamic viscosity of the fluid, and κ is a coefficient varying from 1.04 to 1.65. The parameter κ accounts for the effect of the deviation from the ideal parallel faces conditions. In the above relation, $w^2/12\kappa$ is the intrinsic permeability of the fracture. The existence of fracture besides the longitudinal conductivity may represent an obstacle for fluid flow in the transversal direction because of the potential drop due to the transition from a pore system into an open channel and back into a pore system. Thus, defining the flow potential Φ equal to $\Phi = p + \rho_f (\ddot{u}_i - b_i) x_i$ with x_i denoting the distance

from a datum in ith direction, a jump is admitted in the total flow potential field across the fracture related to transverse fluid flux q_t travelling normal to the discontinuity.

3 The X-FEM formulation of a deformable porous media with strong discontinuity

In order to numerically model a deformable porous media with a strong discontinuity, the extended finite element method is employed by adding appropriate enrichment functions to the standard FE approximation. It must be noted that in the derivation of X-FEM formulation, it is implicitly assumed that the displacement and pressure fields are continuous over the domain of problem, however—necessary modifications must be applied in the variational formulation of X-FEM solution to model the discontinuous displacement field across the fracture and the discontinuous fluid flow in the normal direction to the fracture (Khoei and Nikbakht 2007; Khoei and Karimi 2008; Khoei et al. 2008a). In what follows, the *Divergence theorem* is employed for *discontinuous* problems to provide a mathematical description for the variational formulation of the X-FEM solution. An appropriate term is obtained to incorporate the discontinuity into the X-FEM formulation. The discrete system of X-FEM equation is then obtained by substituting the trial function into the weak form of governing equations.

The *Divergence theorem* for a discontinuous function $\mathbf{F}$ over the domain Ω can be expressed as

$$\int_\Omega \text{div } \mathbf{F} \, d\Omega = \int_\Gamma \mathbf{F} \cdot \mathbf{n}_\Gamma \, d\Gamma - \int_{\Gamma_d} [\![\mathbf{F}]\!] \cdot \mathbf{n}_{\Gamma_d} \, d\Gamma \qquad (7)$$

where $\mathbf{n}_\Gamma$ is the outward unit normal vector to the domain Ω, and the jump of $\mathbf{F}$ is defined as $[\![\mathbf{F}]\!] = \mathbf{F}^+ - \mathbf{F}^-$, where the value of $\mathbf{F}$ on Γ_d^+ and Γ_d^- are denoted by $\mathbf{F}^+$ and $\mathbf{F}^-$, respectively, as shown in Fig. 1. For problems with more than one discontinuity in the domain, Eq. (7) can be written as

$$\int_\Omega \text{div } \mathbf{F} \, d\Omega = \int_\Gamma \mathbf{F} \cdot \mathbf{n}_\Gamma \, d\Gamma - \sum_{i=1}^{NOD} \int_{\Gamma_{d_i}} [\![\mathbf{F}_i]\!] \cdot \mathbf{n}_{\Gamma_{d_i}} \, d\Gamma \qquad (8)$$

where *NOD* is the number of discontinuities in the domain. The above equation can be considered as

an extension of the *Divergence theorem* that provides a mathematical basis for the variational formulation of the X-FEM solution in discontinuous problems.

3.1 The weak formulation of saturated porous media

In order to derive the extended finite element formulation for a deformable porous media with a strong discontinuity, the Divergence theorem for discontinuous problems is employed into the integral formulation of governing Eqs. (1) and (4). The weak form of governing partial differential equations can be obtained by integrating the product of the equilibrium and flow continuity Eqs. (1) and (4) multiplied by admissible test functions over the domain, applying the divergence theorem, imposing the natural boundary conditions, and satisfying the boundary conditions on the discontinuity. It is noteworthy that the mechanical and mass transfer coupling terms naturally appear in the weak form of the equilibrium and flow continuity equations as a result of the presence of discontinuity in the porous medium. In order to obtain the weak form of the equilibrium equation for the fracturing porous medium, the trial functions $\mathbf{u}(\mathbf{x}, t)$ and $p(\mathbf{x}, t)$ are defined to satisfy all essential boundary conditions and to be smooth enough to define the derivatives of equations. In addition, the test functions $\delta\mathbf{u}(\mathbf{x}, t)$ and $\delta p(\mathbf{x}, t)$ are needed to be smooth enough to be vanished on the prescribed strong boundary conditions. The weak form of governing equations can therefore be obtained multiplying the test functions $\delta\mathbf{u}(\mathbf{x}, t)$ and $\delta p(\mathbf{x}, t)$ by Eqs. (1) and (4) and integrating over the domain Ω as

$$\int_{\Omega} \delta\mathbf{u} \left(\nabla \cdot \boldsymbol{\sigma} - \rho\ddot{\mathbf{u}} + \rho\mathbf{b} \right) d\Omega = 0$$

$$\int_{\Omega} \delta p \left(\nabla \cdot \left[\boldsymbol{k}_f \left(-\nabla p - \rho_f \ddot{\mathbf{u}} + \rho_f \mathbf{b} \right) \right] \right.$$

$$\left. + \alpha\nabla \cdot \dot{\mathbf{u}} + \frac{1}{Q}\dot{p} \right) d\Omega = 0 \tag{9}$$

Expanding the above integral equations and using the Divergence theorem (7) for discontinuous problems leads to the following weak form of governing equations as (Khoei 2014)

$$\int_{\Omega} \nabla\delta\mathbf{u} : \boldsymbol{\sigma} d\Omega + \int_{\Omega} \delta\mathbf{u} \cdot \rho\ddot{\mathbf{u}} d\Omega + \int_{\Gamma_d} [\![\delta\mathbf{u}]\!] \boldsymbol{\sigma} \cdot \mathbf{n}_{\Gamma_d} d\Gamma$$

$$- \int_{\Omega} \delta\mathbf{u} \cdot \rho\mathbf{b} d\Omega - \int_{\Gamma_t} \delta\mathbf{u} \cdot \bar{\mathbf{t}} d\Gamma = 0 \tag{10a}$$

$$\int_{\Omega} \nabla\delta p \, \boldsymbol{k}_f \nabla p \, d\Omega + \int_{\Omega} \nabla\delta p \, \boldsymbol{k}_f \cdot \rho_f \ddot{\mathbf{u}} d\Omega$$

$$- \int_{\Gamma_d} \delta p [\![\dot{\mathbf{w}}]\!] \cdot \mathbf{n}_{\Gamma_d} d\Gamma + \int_{\Omega} \delta p \alpha\nabla \cdot \dot{\mathbf{u}} d\Omega$$

$$+ \int_{\Omega} \delta p \frac{1}{Q}\dot{p} d\Omega - \int_{\Omega} \nabla\delta p \, \boldsymbol{k}_f \cdot \rho_f \mathbf{b} d\Omega$$

$$+ \int_{\Gamma_w} \delta p \left(\dot{\mathbf{w}} \cdot \mathbf{n}_\Gamma \right) d\Gamma = 0 \tag{10b}$$

in which the mechanical coupling term in the weak form of Eq. (10a) is computed by assigning the positive and negative sides to Γ_d and imposing the internal boundary condition on the discontinuity. Moreover, the mass transfer coupling term in the weak form of the continuity Eq. (10b) is obtained by imposing the boundary condition on the discontinuity. In Eq. (10b), the term $[\![\dot{\mathbf{w}}]\!] \cdot \mathbf{n}_{\Gamma_d} = \bar{q}_d$ corresponds to fluid flow from the crack normal to the cavity.
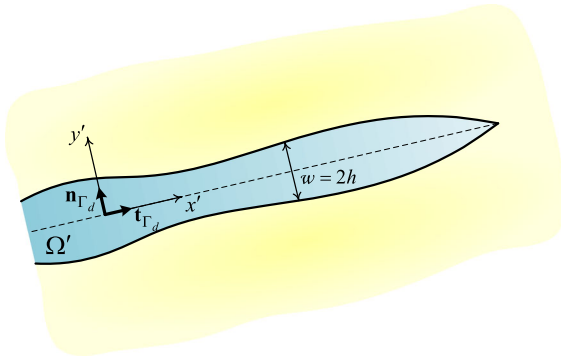
3.2 The weak formulation of fractured media

In order to derive a relation for the mass transfer coupling term emerging in the weak form of the flow continuity Eq. (10b) within the porous medium surrounding the fracture, the flow continuity of fluid inside the fracture is employed using Eq. (5). The weak form of flow continuity equation within the fracture can be obtained by multiplying the test functions $\delta p(\mathbf{x}, t)$ by Eq. (5) and integrating over the domain of the discontinuity Ω' (Fig. 2) as

$$\int_{\Omega'} \delta p \left(\nabla \cdot \dot{\mathbf{w}} + \alpha\nabla \cdot \dot{\mathbf{u}} + \frac{1}{K_f}\dot{p} \right) d\Omega = 0 \tag{11}$$

or

$$\int_{\Omega'} \delta p \left(\nabla \cdot \left[k_{f_d} \left(-\nabla p - \rho_f \ddot{\mathbf{u}} + \rho_f \mathbf{b} \right) \right] + \alpha\nabla \cdot \dot{\mathbf{u}} \right.$$

$$\left. + \frac{1}{K_f}\dot{p} \right) d\Omega = 0 \tag{12}$$

The implementation of the divergence theorem for discontinuous problems and the incorporation of the

Fig. 2 The geometry of the fluid flow inside the fracture

Darcy relation lead to the weak form of continuity equation of flow within the fracture as

$$
\int_{\Omega'} \nabla \delta p k_{f_d} \nabla p d\Omega + \int_{\Omega'} \nabla \delta p k_{f_d} \rho_f \ddot{\mathbf{u}} d\Omega
$$

$$
- \int_{\Gamma_d} \delta p [\![\dot{\mathbf{w}}]\!] \cdot \mathbf{n}_{\Gamma_d} d\Gamma
$$

$$
+ \int_{\Omega'} \delta p \alpha \nabla \cdot \dot{\mathbf{u}} d\Omega + \int_{\Omega'} \delta p \frac{1}{K_f} \dot{p} d\Omega
$$

$$
- \int_{\Omega} \nabla \delta p k_{f_d} \rho_f \mathbf{b} d\Omega = 0 \tag{13}
$$

Hence, the mass transfer coupling term in the weak form of the flow continuity Eq. (10b) can be obtained from the weak form of the flow continuity Eq. (13) within the fracture as

$$
\int_{\Gamma_d} \delta p [\![\dot{\mathbf{w}}]\!] \cdot \mathbf{n}_{\Gamma_d} d\Gamma = - \underbrace{\int_{\Omega'} \nabla \delta p k_{f_d} \nabla p d\Omega}_{\text{integral(I)}}
$$

$$
- \underbrace{\int_{\Omega'} \nabla \delta p k_{f_d} \rho_f \ddot{\mathbf{u}} d\Omega}_{\text{integral(II)}} - \underbrace{\int_{\Omega'} \delta p \alpha \nabla \cdot \dot{\mathbf{u}} d\Omega}_{\text{integral(III)}}
$$

$$
- \underbrace{\int_{\Omega'} \delta p \frac{1}{K_f} \dot{p} d\Omega}_{\text{integral(IV)}} + \underbrace{\int_{\Omega} \nabla \delta p k_{f_d} \rho_f \mathbf{b} d\Omega}_{\text{integral(V)}} \tag{14}
$$

In order to evaluate the mass transfer coupling term in Eq. (14), the integral terms (I)–(V) are calculated in the local Cartesian coordinate system (x', y'), where the directions of x' and y' are aligned with the tangent and normal unit vectors to the discontinuity, $\mathbf{t}_{\Gamma_d}$ and

$\mathbf{n}_{\Gamma_d}$ respectively, as shown in Fig. 2. The integrals over the domain of the discontinuity Ω' are performed in the local coordinate system, in which the integral over the cross section of the discontinuity is evaluated by ignoring the variation of fluid pressure across the discontinuity width since the width of the discontinuity $2h$ is insignificant relative to its length. As a result, the fluid pressure as well as its corresponding test function is assumed to be uniform over the cross section of the discontinuity. Hence, the derivation of integrals (I)–(V) in Eq. (14) can be obtained as

$$
\underbrace{\int_{\Omega'} \nabla \delta p k_{f_d} \nabla p d\Omega}_{\text{integral(I)}} = \int_{\Gamma_d} k_{f_d} (2h) \frac{\partial \delta p}{\partial x'} \frac{\partial p}{\partial x'} d\Gamma \tag{15a}
$$

$$
\underbrace{\int_{\Omega'} \nabla \delta p k_{f_d} \rho_f \ddot{\mathbf{u}} d\Omega}_{\text{integral(II)}} = \int_{\Gamma_d} k_{f_d} \rho_f (2h) \frac{\partial \delta p}{\partial x'} \langle \ddot{u}_{x'} \rangle d\Gamma
$$

$$
\tag{15b}
$$

$$
\underbrace{\int_{\Omega'} \delta p \alpha \nabla \cdot \dot{\mathbf{u}} d\Omega}_{\text{integral(III)}} = \int_{\Gamma_d} \delta p \alpha (2h) \left\langle \frac{\partial \dot{u}_{x'}}{\partial x'} \right\rangle d\Gamma
$$

$$
+ \int_{\Gamma_d} \delta p \alpha [\![\dot{u}_{y'}]\!] d\Gamma \tag{15c}
$$

$$
\underbrace{\int_{\Omega'} \delta p \frac{1}{K_f} \dot{p} d\Omega}_{\text{integral(IV)}} = \int_{\Gamma_d} \delta p (2h) \frac{1}{K_f} \dot{p} d\Gamma \tag{15d}
$$

$$
\underbrace{\int_{\Omega} \nabla \delta p k_{f_d} \rho_f \mathbf{b} d\Omega}_{\text{integral(V)}} = \int_{\Gamma_d} k_{f_d} \rho_f (2h) \frac{\partial \delta p}{\partial x'} b_{x'} d\Gamma \tag{15e}
$$

In above equations, $\dot{u}_{x'}$ and $\dot{u}_{y'}$ are the components of the solid velocity vector projected on the longitudinal and transversal axes, respectively. It is assumed that the velocity component of the solid phase in the longitudinal direction $\dot{u}_{x'}$ varies linearly with y' over the width of the discontinuity $2h$, so its derivative with respect to x' also varies linearly with y'. Similar to that assumed for the solid velocity in the tangential direction of the discontinuity, the solid acceleration in the tangential direction $\ddot{u}_{x'}$ also varies linearly with y'. As noted earlier, the fluid pressure and its corresponding test function are assumed to be uniform across the width of the discontinuity, so their derivatives in the tangen-

tial direction do not vary with y', and their derivatives in the normal direction vanish. Furthermore, the tangential derivatives in above equations are analytically integrated over the width of the discontinuity $2h$, in which $\langle \varXi \rangle = (\varXi^+ + \varXi^-)/2$ is defined as the average of corresponding values at the discontinuity faces.

Substituting the constituents of Eq. (14) and rearranging it, the mass transfer coupling term appeared in the weak form of the flow continuity Eq. (10b) in the porous medium can be obtained as

$$
\int_{\Gamma_d} \delta p [\![\dot{\mathbf{w}}]\!] \cdot \mathbf{n}_{\Gamma_d} d\Gamma = -\int_{\Gamma_d} k_{f_d}(2h) \frac{\partial \delta p}{\partial x'} \frac{\partial p}{\partial x'} d\Gamma
$$
$$
-\int_{\Gamma_d} k_{f_d} \rho_f (2h) \frac{\partial \delta p}{\partial x'} \langle \ddot{u}_{x'} \rangle d\Gamma
$$
$$
-\int_{\Gamma_d} \delta p \alpha (2h) \left\langle \frac{\partial \dot{u}_{x'}}{\partial x'} \right\rangle d\Gamma - \int_{\Gamma_d} \delta p \alpha [\![\dot{u}_{y'}]\!] d\Gamma
$$
$$
-\int_{\Gamma_d} \delta p (2h) \frac{1}{K_f} \dot{p} d\Gamma + \int_{\Gamma_d} k_{f_d} \rho_f (2h) \frac{\partial \delta p}{\partial x'} b_{x'} d\Gamma
$$
$$
\tag{16}
$$

The above equation presents an expression for the leak-off from the crack into the porous media. Since the flow within the fracture is generally assumed to be incompressible, the integral (IV) can be removed from Eq. (16). In order to model the flow within the fracture, a viscous Newtonian fluid flow is assumed between the crack faces, in which the fracture permeability is defined according to (6) based on the cubic law as $k_{f_d} = (2h)^2/12\kappa\mu_f$. It must be noted that this relation is only valid if the fluid regime inside the cavity is laminar.

4 Discretization of governing equations

In this section, the weak form of the equilibrium and flow continuity equations of the porous medium obtained in preceding section is used to derive the discrete form of governing equations by discretization of the governing equations first in the spatial domain employing the extended finite element method and then in the time domain applying the generalized Newmark scheme. The resulting system of fully coupled nonlinear equations is finally solved using the Newton–Raphson procedure.

4.1 Approximation of the displacement and pressure fields

In order to discretize the integral Eq. (10), the extended finite element method is employed in the spatial domain to obtain the values of $\mathbf{u}(\mathbf{x}, t)$ and $p(\mathbf{x}, t)$. In the X-FEM method, the conventional FEM shape functions are enriched using proper enrichment functions based on the type of discontinuity. The displacement and pressure fields are enriched based on the analytical solutions to make the approximations capable of tracking the discontinuities. In order to capture the hydro-mechanical coupling associated with the tractions acting on the crack edges and the fluid leak-off from the fracture into the domain, the displacement and fluid pressure fields are enhanced using appropriate enrichment functions. To describe the displacement jump across the fracture, the displacement field is assumed to be discontinuous over the crack edges. In addition, to present the fluid flow jump normal to the fracture, the fluid pressure field is assumed to be continuous, while its gradient normal to the fracture be discontinuous over the crack edges. Thus, the displacement discontinuity over the crack edges is modeled using the Heaviside and crack-tip asymptotic functions, and the fluid pressure is modeled using the modified level-set function to capture the discontinuity on the gradient of fluid pressure normal to the fracture.

The enriched approximation of the extended finite element method for the displacement field $\mathbf{u}(\mathbf{x}, t)$ can be written as (Belytschko et al. 2003)

$$
\mathbf{u}(\mathbf{x}, t) \approx \mathbf{u}^h(\mathbf{x}, t) = \sum_{I \in \mathcal{N}} N_{uI}(x) \bar{u}_I(t)
$$
$$
+ \sum_{J \in \mathcal{N}^{dis}} N_{uJ}(\mathbf{x}) \left(H(\varphi(\mathbf{x})) - H(\varphi(\mathbf{x}_J)) \right) \bar{\mathbf{a}}_J(t)
$$
$$
+ \sum_{K \in \mathcal{N}^{tip}} N_{uK}(\mathbf{x}) \sum_{\alpha=1}^{4} (\mathcal{B}_\alpha(\mathbf{x}) - \mathcal{B}_\alpha(x_K)) \bar{\mathbf{b}}_{\alpha K}(t)
$$
$$
\tag{17}
$$

where $\mathcal{N}$ is the set of all nodal points, $\mathcal{N}^{dis}$ is the set of enriched nodes whose support is bisected by the crack, and $\mathcal{N}^{tip}$ is the set of nodes which contain the crack-tip in the support of their shape functions enriched by the asymptotic functions. In the above relation, $\bar{\mathbf{u}}_I(t)$ are the unknown standard nodal displacements at Ith node, $\bar{\mathbf{a}}_J(t)$ are the unknown enriched nodal degrees-of-freedom associated with the Heaviside enrichment function at node J, and $\bar{b}_{\alpha K}(t)$ are

the additional enriched nodal degrees-of-freedom associated with the asymptotic functions at node K. In relation (17), $N_u(x)$ denote the standard displacement shape functions, $H(\varphi(x))$ is the Heaviside jump function used to model the discontinuity due to different displacement fields on either sides of the crack, and $\mathcal{B}_\alpha(x)$ are the asymptotic functions extracted from the analytical solution and used to model the displacement field at the crack-tip region. The asymptotic tip functions $\mathcal{B}_\alpha(x)$ and the Heaviside jump function $H(\varphi(x))$ are defined as (Bordas and Legay 2005)

$$
\begin{aligned}
\mathcal{B}(r, \theta) &= \{\mathcal{B}_1, \mathcal{B}_2, \mathcal{B}_3, \mathcal{B}_4\} \\
&= \left\{ \sqrt{r} \sin\frac{\theta}{2}, \sqrt{r} \cos\frac{\theta}{2}, \sqrt{r} \sin\frac{\theta}{2} \sin\theta, \sqrt{r} \cos\frac{\theta}{2} \sin\theta \right\}
\end{aligned}
\tag{18}
$$

and

$$
H(\varphi(x)) = \begin{cases} +1 & \varphi(x) \geq 0 \\ 0 & \varphi(x) < 0 \end{cases}
\tag{19}
$$

where $\varphi(x)$ is the signed distance function defined based on the absolute value of level set function as $\varphi(x) = \min \|x - x^*\| \, \text{sign}\left((x - x^*) \cdot \mathbf{n}_{\Gamma_d}\right)$, where x^* is a point on the discontinuity which has the closest distance from the point x, and $\mathbf{n}_{\Gamma_d}$ is the normal vector to the contact interface at point x^*. It must be noted that the use of Heaviside function (19) instead of the sign of the level-set function is common in the literature (De Borst et al. 2006), and both lead to identical results as they span the same approximation space (Fries and Belytschko 2010).

The enriched approximation of the extended finite element method for the pressure field $p(x, t)$ can be written as (Réthoré et al. 2007a)

$$
\begin{aligned}
p(x, t) &\approx p^h(x, t) = \sum_{I \in \mathcal{N}} N_{pI}(x) \bar{p}_I(t) \\
&+ \sum_{J \in \mathcal{N}^{dis}} N_{pJ}(x) \left(\psi(x) - \psi(x_J)\right) \bar{c}_J(t)
\end{aligned}
\tag{20}
$$

where $\bar{p}_I(t)$ is the unknown standard nodal pressure at Ith node, and $\bar{c}_J(t)$ is the unknown enriched nodal degrees-of-freedom associated with the modified level-set function at node J. In the above relation, $N_p(x)$ are the standard pressure shape functions, and $\psi(x)$ is the modified level-set function defined as

$$
\psi(x) = \sum_{I \in \mathcal{N}^{dis}} N_{pI}(x) |\varphi_I| - \left| \sum_{I \in \mathcal{N}^{dis}} N_{pI}(x) \varphi_I \right|
\tag{21}
$$

where φ_I are the nodal values of the level set function. The above enrichment function has a ridge centered on the interpolated interface and vanishes in elements not containing the material interface. This enrichment function is used since the resulting enrichment function is zero in the blending elements, and the unwanted terms appearing in the approximating space of the blending elements are avoided. It must be noted that the above enrichment is only required in the elements where the discontinuity on the gradient of fluid pressure needs to be captured. In the above relation, the enrichment function is continuous across the fracture, while its gradient is discontinuous in the normal direction to the discontinuity. Possessing this desirable property, the chosen enrichment function enables the approximate pressure field to be discontinuous in its normal derivative across the discontinuity, accounting for the leak-off of the fluid from the discontinuity. In Fig. 3, the enriched nodal points of the displacement and pressure fields are presented for a discontinuous domain according to the Heaviside jump function, asymptotic tip functions, and the modified level-set function.
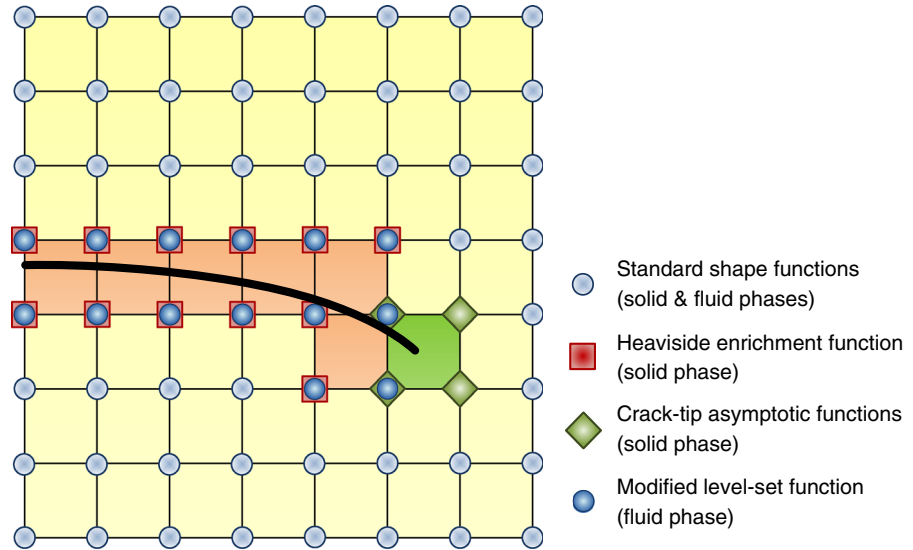
Finally, the enriched finite element approximation of the displacement and pressure fields (17) and (20) can be symbolically written in the following form

$$
\mathbf{u}^h(x, t) = \mathbf{N}_u^{std}(x)\bar{\mathbf{u}}(t) + \mathbf{N}_u^{Hev}(x)\bar{\mathbf{a}}(t) + \mathbf{N}_u^{tip}(x)\bar{\mathbf{b}}(t)
\tag{22}
$$

$$
p^h(x, t) = \mathbf{N}_p^{std}(x)\bar{\mathbf{p}}(t) + \mathbf{N}_p^{abs}(x)\bar{\mathbf{c}}(t)
\tag{23}
$$

where $\mathbf{N}_u^{std}(x)$ is the matrix of displacement shape functions that include the standard piecewise polynomial shape functions, $\mathbf{N}_u^{Hev}(x)$ is the matrix of enriched shape functions associated with the Heaviside function, $\mathbf{N}_u^{tip}(x)$ is the matrix of enriched shape functions associated with the asymptotic tip functions, $\bar{\mathbf{u}}(t)$ is the vector of standard displacement degrees of freedom, $\bar{\mathbf{a}}(t)$ is the vector of enriched displacement degrees of freedom associated with the Heaviside function, and $\bar{\mathbf{b}}(t)$ is the vector of enriched displacement degrees of freedom associated with the asymptotic tip functions. In relation (23), $\mathbf{N}_p^{std}(x)$ is the matrix of pressure shape functions, $\mathbf{N}_p^{abs}(x)$ is the matrix of enriched shape functions associated with the modified level-set function, $\bar{\mathbf{p}}(t)$ is the vector of pressure nodal degrees of freedom, and $\bar{\mathbf{c}}(t)$ is the vector of enriched nodal degrees of freedom associated with the modified level-set function.

Fig. 3 The enriched nodal points of the displacement and pressure fields in porous media

Standard shape functions (solid & fluid phases)

Heaviside enrichment function (solid phase)

Crack-tip asymptotic functions (solid phase)

Modified level-set function (fluid phase)

4.2 The X-FEM spatial discretization

The discrete form of integral Eq. (10) in the framework of X-FEM formulation can be obtained using the test and trial functions of the enriched displacement and pressure fields. Applying the trial functions of enriched displacement and pressure fields (22) and (23) together with the test functions of displacement and pressure fields $\delta\mathbf{u}(\mathbf{x}, t)$ and $\delta p(\mathbf{x}, t)$, which are respectively defined in the same enriched approximating space as the approximate displacement and fluid pressure fields as

$$\delta\mathbf{u}^h(\mathbf{x}, t) = \mathbf{N}_u^{std}(\mathbf{x})\delta\bar{\mathbf{u}}(t) + \mathbf{N}_u^{Hev}(\mathbf{x})\delta\bar{\mathbf{a}}(t) + \mathbf{N}_u^{tip}(\mathbf{x})\delta\bar{\mathbf{b}}(t) \tag{24}$$

$$\delta p^h(\mathbf{x}, t) = \mathbf{N}_p^{std}(\mathbf{x})\delta\bar{\mathbf{p}}(t) + N_p^{abs}(\mathbf{x})\delta\bar{\mathbf{c}}(t) \tag{25}$$

and satisfying the necessity that the weak form should hold for all kinematically admissible test functions, the discretized form of integral Eq. (10) can therefore be obtained according to the Bubnov–Galerkin technique as

$$\begin{pmatrix} \mathbf{M}_{uu} & \mathbf{M}_{ua} & \mathbf{M}_{ub} \\ \mathbf{M}_{au} & \mathbf{M}_{aa} & \mathbf{M}_{ab} \\ \mathbf{M}_{bu} & \mathbf{M}_{ba} & \mathbf{M}_{bb} \end{pmatrix} \begin{Bmatrix} \ddot{\bar{\mathbf{u}}} \\ \ddot{\bar{\mathbf{a}}} \\ \ddot{\bar{\mathbf{b}}} \end{Bmatrix} + \begin{pmatrix} \mathbf{K}_{uu} & \mathbf{K}_{ua} & \mathbf{K}_{ub} \\ \mathbf{K}_{au} & \mathbf{K}_{aa} & \mathbf{K}_{ab} \\ \mathbf{K}_{bu} & \mathbf{K}_{ba} & \mathbf{K}_{bb} \end{pmatrix} \begin{Bmatrix} \bar{\mathbf{u}} \\ \bar{\mathbf{a}} \\ \bar{\mathbf{b}} \end{Bmatrix}$$
$$- \begin{pmatrix} \mathbf{Q}_{up} & \mathbf{Q}_{uc} \\ \mathbf{Q}_{ap} & \mathbf{Q}_{ac} \\ \mathbf{Q}_{bp} & \mathbf{Q}_{bc} \end{pmatrix} \begin{Bmatrix} \bar{\mathbf{p}} \\ \bar{\mathbf{c}} \end{Bmatrix} + \begin{Bmatrix} \mathbf{f}_u^{int} \\ \mathbf{f}_a^{int} \\ \mathbf{f}_b^{int} \end{Bmatrix} - \begin{Bmatrix} \mathbf{f}_u^{ext} \\ \mathbf{f}_a^{ext} \\ \mathbf{f}_b^{ext} \end{Bmatrix} = \mathbf{0}$$

$$\begin{pmatrix} \mathbf{C}_{pu} & \mathbf{C}_{pa} & \mathbf{C}_{pb} \\ \mathbf{C}_{cu} & \mathbf{C}_{ca} & \mathbf{C}_{cb} \end{pmatrix} \begin{Bmatrix} \ddot{\bar{\mathbf{u}}} \\ \ddot{\bar{\mathbf{a}}} \\ \ddot{\bar{\mathbf{b}}} \end{Bmatrix} + \begin{pmatrix} \mathbf{Q}_{up}^T & \mathbf{Q}_{ap}^T & \mathbf{Q}_{bp}^T \\ \mathbf{Q}_{uc}^T & \mathbf{Q}_{ac}^T & \mathbf{Q}_{bc}^T \end{pmatrix} \begin{Bmatrix} \dot{\bar{\mathbf{u}}} \\ \dot{\bar{\mathbf{a}}} \\ \dot{\bar{\mathbf{b}}} \end{Bmatrix}$$
$$+ \begin{pmatrix} \mathbf{H}_{pp} & \mathbf{H}_{pc} \\ \mathbf{H}_{cp} & \mathbf{H}_{cc} \end{pmatrix} \begin{Bmatrix} \bar{\mathbf{p}} \\ \bar{\mathbf{c}} \end{Bmatrix} + \begin{pmatrix} \mathbf{S}_{pp} & \mathbf{S}_{pc} \\ \mathbf{S}_{cp} & \mathbf{S}_{cc} \end{pmatrix} \begin{Bmatrix} \dot{\bar{\mathbf{p}}} \\ \dot{\bar{\mathbf{c}}} \end{Bmatrix}$$
$$- \begin{Bmatrix} \mathbf{q}_p^{int} \\ \mathbf{q}_c^{int} \end{Bmatrix} - \begin{Bmatrix} \mathbf{q}_p^{ext} \\ \mathbf{q}_c^{ext} \end{Bmatrix} = \mathbf{0} \tag{26}$$

where the mass matrix $\mathbf{M}$, stiffness matrix $\mathbf{K}$, coupling matrix $\mathbf{Q}$, permeability matrix $\mathbf{H}$, compressibility matrix $\mathbf{S}$, and external force vectors $\mathbf{f}^{ext}$ and $\mathbf{q}^{ext}$ are defined as

$$\mathbf{M}_{\alpha\beta} = \int_{\Omega} \left(\mathbf{N}_u^\alpha\right)^T \rho \mathbf{N}_u^\beta d\Omega$$

$$\mathbf{K}_{\alpha\beta} = \int_{\Omega} \left(\mathbf{B}_u^\alpha\right)^T \mathbf{D}\mathbf{B}_u^\beta d\Omega$$

$$\mathbf{Q}_{\alpha\gamma} = \int_{\Omega} \left(\mathbf{B}_u^\alpha\right)^T \alpha \, \mathbf{m}\mathbf{N}_p^\gamma d\Omega$$

$$\mathbf{f}_\alpha^{ext} = \int_{\Omega} \left(\mathbf{N}_u^\alpha\right)^T \rho \mathbf{b} d\Omega + \int_{\Gamma_t} \left(\mathbf{N}_u^\alpha\right)^T \bar{\mathbf{t}} d\Gamma \tag{27}$$

and

$$\mathbf{C}_{\delta\beta} = \int_{\Omega} \left(\nabla\mathbf{N}_p^\delta\right)^T \mathbf{k}_f \cdot \rho_f \mathbf{N}_u^\beta d\Omega$$

$$\mathbf{H}_{\delta\gamma} = \int_{\Omega} \left(\nabla\mathbf{N}_p^\delta\right)^T \mathbf{k}_f (\nabla\mathbf{N}_p^\gamma) d\Omega$$

$$\mathbf{S}_{\delta\gamma} = \int_{\Omega} \left(\mathbf{N}_p^\delta\right)^T \frac{1}{Q}\mathbf{N}_p^\gamma d\Omega$$

$$\mathbf{q}_\delta^{\text{ext}} = \int_\Omega \left(\nabla \mathbf{N}_p^\delta\right)^T \mathbf{k}_f \cdot \rho_f \mathbf{b} d\Omega - \int_{\Gamma_w} \left(\mathbf{N}_p^\delta\right)^T \bar{q} d\Gamma \tag{28}$$

where $(\alpha, \beta) \in (std, Hev, tip)$ denote the 'standard', 'Heaviside' and 'asymptotic-tip' functions of displacement field and, $(\delta, \gamma) \in (std, abs)$ denote the 'standard' and 'modified level-set' functions of pressure field. In above definitions, $\mathbf{m}$ is the vector of delta Dirac function defined as $\mathbf{m} = \left\{ 1\ 1\ 0 \right\}^T$.

In order to discretize the mechanical and mass transfer couplings between the fracture and the porous medium in integral Eq. (10), the interfacial force vector $\mathbf{f}_\alpha^{\text{int}}$ due to the fluid pressure exerted on the fracture faces by injecting a viscous fluid into the fracture, and the flux vectors $\mathbf{q}_\delta^{\text{int}}$ due to the fluid exchange between the fracture and the surrounding permeable porous medium in Eq. (26) can be obtained as

$$\mathbf{f}_\alpha^{\text{int}} = \int_{\Gamma_d} [\![\mathbf{N}_u^\alpha]\!]^T \boldsymbol{\sigma} \cdot \mathbf{n}_{\Gamma_d} d\Gamma = -\int_{\Gamma_d} [\![\mathbf{N}_u^\alpha]\!]^T p \cdot \mathbf{n}_{\Gamma_d} d\Gamma \tag{29}$$

where $\alpha \in (std, Hev, tip)$, and

$$\begin{aligned}
\mathbf{q}_\delta^{\text{int}} &= \int_{\Gamma_d} \left(\mathbf{N}_p^\delta\right)^T [\![\dot{\mathbf{w}}]\!] \cdot \mathbf{n}_{\Gamma_d} d\Gamma = \int_{\Gamma_d} \left(\mathbf{N}_p^\delta\right)^T \bar{q}_d d\Gamma \\
&= -\int_{\Gamma_d} \left(\nabla \mathbf{N}_p^\delta\right)^T \cdot \mathbf{t}_{\Gamma_d} k_{f_d} (2h) \nabla p \cdot \mathbf{t}_{\Gamma_d} d\Gamma \\
&\quad - \int_{\Gamma_d} \left(\nabla \mathbf{N}_p^\delta\right)^T \cdot \mathbf{t}_{\Gamma_d} k_{f_d} \rho_f (2h) \langle \ddot{\mathbf{u}} \rangle \cdot \mathbf{t}_{\Gamma_d} d\Gamma \\
&\quad - \int_{\Gamma_d} \left(\mathbf{N}_p^\delta\right)^T \alpha (2h) \mathbf{t}_{\Gamma_d} \cdot \langle \nabla \dot{\mathbf{u}} \rangle \cdot \mathbf{t}_{\Gamma_d} d\Gamma \\
&\quad - \int_{\Gamma_d} \left(\mathbf{N}_p^\delta\right)^T \alpha [\![\dot{\mathbf{u}}]\!] \cdot \mathbf{n}_{\Gamma_d} d\Gamma \\
&\quad - \int_{\Gamma_d} \left(\mathbf{N}_p^\delta\right)^T (2h) \frac{1}{K_f} \dot{p} d\Gamma \\
&\quad + \int_{\Gamma_d} \left(\nabla \mathbf{N}_p^\delta\right)^T \cdot \mathbf{t}_{\Gamma_d} k_{f_d} \rho_f (2h) \mathbf{b} \cdot \mathbf{t}_{\Gamma_d} d\Gamma \tag{30}
\end{aligned}$$

where $\delta \in (std, abs)$. Finally, the X-FEM discretization Eq. (26) can be rewritten as

$$\begin{aligned}
&\mathbf{M}\ddot{\bar{\mathbb{U}}} + \mathbf{K}\bar{\mathbb{U}} - \mathbf{Q}\bar{\mathbb{P}} + \mathbf{f}_\mathbb{U}^{int} - \mathbf{f}_\mathbb{U}^{\text{ext}} = \mathbf{0} \\
&\mathbf{C}\ddot{\bar{\mathbb{U}}} + \mathbf{Q}^T \dot{\bar{\mathbb{U}}} + \mathbf{H}\bar{\mathbb{P}} + \mathbf{S}\dot{\bar{\mathbb{P}}} - \mathbf{q}_\mathbb{P}^{int} - \mathbf{q}_\mathbb{P}^{\text{ext}} = \mathbf{0} \tag{31}
\end{aligned}$$

where $\bar{\mathbb{U}} = \langle \bar{\mathbf{u}}, \bar{\mathbf{a}}, \bar{\mathbf{b}} \rangle$ and $\bar{\mathbb{P}} = \langle \bar{\mathbf{p}}, \bar{\mathbf{c}} \rangle$ are the complete set of the standard and enriched degrees-of-freedom of displacement and pressure fields, respectively.

4.3 The time domain discretization and solution procedure

In order to complete the numerical solution of FE equations, it is necessary to integrate the time differential Eqs. (31) in time. The well-known generalized Newmark GN22 scheme is employed for the displacement field $\bar{\mathbb{U}}$ and the GN11 method for the pressure field $\bar{\mathbb{P}}$. The link between the successive values of the unknown field variables at time $t_{n+1} = t_n + \Delta t$ and the known field variables at time t_n can be established as

$$\begin{aligned}
\ddot{\bar{\mathbb{U}}}_{n+1} &= \frac{1}{\beta \Delta t^2} \left(\bar{\mathbb{U}}_{n+1} - \bar{\mathbb{U}}_n \right) \\
&\quad - \frac{1}{\beta \Delta t} \dot{\bar{\mathbb{U}}}_n - \left(\frac{1}{2\beta} - 1 \right) \ddot{\bar{\mathbb{U}}}_n \\
\dot{\bar{\mathbb{U}}}_{n+1} &= \frac{\gamma}{\beta \Delta t} \left(\bar{\mathbb{U}}_{n+1} - \bar{\mathbb{U}}_n \right) \\
&\quad - \left(\frac{\gamma}{\beta} - 1 \right) \dot{\bar{\mathbb{U}}}_n - \Delta t \left(\frac{\gamma}{2\beta} - 1 \right) \ddot{\bar{\mathbb{U}}}_n \tag{32a}
\end{aligned}$$

and

$$\dot{\bar{\mathbb{P}}}_{n+1} = \frac{1}{\theta \Delta t} \left(\bar{\mathbb{P}}_{n+1} - \bar{\mathbb{P}}_n \right) - \left(\frac{1}{\theta} - 1 \right) \dot{\bar{\mathbb{P}}}_n \tag{32b}$$

where β, γ and θ are parameters, which are usually chosen in the range of 0–1. However, for unconditionally stability of the time integration procedure, it is required that $\gamma \geq 0.5$, $\beta \geq 0.25(0.5 + \gamma)^2$ and $\theta \geq 0.5$. In above relations, $\bar{\mathbb{U}}_n$, $\dot{\bar{\mathbb{U}}}_n$ and $\ddot{\bar{\mathbb{U}}}_n$ denote the known values of displacement, velocity and acceleration of the standard and enriched degrees of freedom at time t_n, and $\bar{\mathbb{P}}_n$ and $\dot{\bar{\mathbb{P}}}_n$ are the known values of pressure and gradient of pressure of the standard and enriched DOFs at time t_n. Substituting relations (32a) and (32b) into the spatial discrete Eq. (31), the following nonlinear equation can be achieved as

$$\begin{aligned}
\boldsymbol{\Psi}_{\mathbb{U}_{n+1}} &= \frac{1}{\beta \Delta t^2} \mathbf{M}\bar{\mathbb{U}}_{n+1} + \mathbf{K}\bar{\mathbb{U}}_{n+1} \\
&\quad - \mathbf{Q}\bar{\mathbb{P}}_{n+1} + \mathbf{f}_{\mathbb{U}_{n+1}}^{\text{int}} - \mathbf{G}_{\mathbb{U}_{n+1}} = \mathbf{0} \\
\boldsymbol{\Psi}_{\mathbb{P}_{n+1}} &= \frac{1}{\beta \Delta t^2} \mathbf{C}\bar{\mathbb{U}}_{n+1} + \frac{\gamma}{\beta \Delta t} \mathbf{Q}^T \bar{\mathbb{U}}_{n+1} + \mathbf{H}\bar{\mathbb{P}}_{n+1} \\
&\quad + \frac{1}{\theta \Delta t} \mathbf{S}\bar{\mathbb{P}}_{n+1} - \mathbf{q}_{\mathbb{P}_{n+1}}^{\text{int}} - \mathbf{G}_{\mathbb{P}_{n+1}} = 0 \tag{33}
\end{aligned}$$

where $\mathbf{G}_{\mathbb{U}_{n+1}}$ and $\mathbf{G}_{\mathbb{P}_{n+1}}$ are the vector of known values at time t_n defined as

$$
\mathbf{G}_{\mathbb{U}_{n+1}} = \mathbf{f}_{\mathbb{U}_{n+1}}^{\text{ext}} + \mathbf{M}\left(\frac{1}{\beta \Delta t^2}\bar{\mathbb{U}}_n + \frac{1}{\beta \Delta t}\dot{\bar{\mathbb{U}}}_n + \left(\frac{1}{2\beta} - 1\right)\ddot{\bar{\mathbb{U}}}_n\right)
$$

$$
\mathbf{G}_{\mathbb{P}_{n+1}} = \mathbf{q}_{\mathbb{P}_{n+1}}^{\text{ext}} + \mathbf{C}\left(\frac{1}{\beta \Delta t^2}\bar{\mathbb{U}}_n + \frac{1}{\beta \Delta t}\dot{\bar{\mathbb{U}}}_n + \left(\frac{1}{2\beta} - 1\right)\ddot{\bar{\mathbb{U}}}_n\right)
$$
$$
+ \mathbf{Q}^T\left(\frac{\gamma}{\beta \Delta t}\bar{\mathbb{U}}_n + \left(\frac{\gamma}{\beta} - 1\right)\dot{\bar{\mathbb{U}}}_n + \Delta t\left(\frac{\gamma}{2\beta} - 1\right)\ddot{\bar{\mathbb{U}}}_n\right)
$$
$$
+ \mathbf{S}\left(\frac{1}{\theta \Delta t}\bar{\mathbb{P}}_n + \left(\frac{1}{\theta} - 1\right)\dot{\bar{\mathbb{P}}}_n\right) \tag{34}
$$

The set of nonlinear Eq. (33) can be solved using an appropriate approach, such as the Newton–Raphson iterative algorithm to linearize the nonlinear system of equations. Note that the nonlinearity of the above system of equations is induced due to interfacial terms, as they involve higher order permeability introduced via the second order aperture dependent cubic law. By expanding Eq. (33) with the first-order truncated Taylor series, the following linear approximation can be obtained as

$$
\left\{\begin{matrix} \boldsymbol{\Psi}_{\mathbb{U}_{n+1}}^{i+1} \\ \boldsymbol{\Psi}_{\mathbb{P}_{n+1}}^{i+1} \end{matrix}\right\} = \left\{\begin{matrix} \boldsymbol{\Psi}_{\mathbb{U}_{n+1}}^{i} \\ \boldsymbol{\Psi}_{\mathbb{P}_{n+1}}^{i} \end{matrix}\right\} + \left[\begin{matrix} \dfrac{\partial \boldsymbol{\Psi}_{\mathbb{U}}}{\partial \bar{\mathbb{U}}} & \dfrac{\partial \boldsymbol{\Psi}_{\mathbb{U}}}{\partial \bar{\mathbb{P}}} \\ \dfrac{\partial \boldsymbol{\Psi}_{\mathbb{P}}}{\partial \bar{\mathbb{U}}} & \dfrac{\partial \boldsymbol{\Psi}_{\mathbb{P}}}{\partial \bar{\mathbb{P}}} \end{matrix}\right]_{n+1}^{i}
$$
$$
\left\{\begin{matrix} d\bar{\mathbb{U}}_{n+1}^{i} \\ d\bar{\mathbb{P}}_{n+1}^{i} \end{matrix}\right\} = \mathbf{0} \tag{35}
$$

where the Jacobian matrix $\mathbf{J}$ in Eq. (35) can be obtained as

$$
\mathbf{J} = \left[\begin{matrix} \dfrac{\partial \boldsymbol{\Psi}_{\mathbb{U}}}{\partial \bar{\mathbb{U}}} & \dfrac{\partial \boldsymbol{\Psi}_{\mathbb{U}}}{\partial \bar{\mathbb{P}}} \\ \dfrac{\partial \boldsymbol{\Psi}_{\mathbb{P}}}{\partial \bar{\mathbb{U}}} & \dfrac{\partial \boldsymbol{\Psi}_{\mathbb{P}}}{\partial \bar{\mathbb{P}}} \end{matrix}\right]
$$
$$
= \left[\begin{matrix} \dfrac{1}{\beta \Delta t^2}\mathbf{M} + \mathbf{K} + \dfrac{\partial \mathbf{f}_{\mathbb{U}}^{\text{int}}}{\partial \bar{\mathbb{U}}} & -\mathbf{Q} + \dfrac{\partial \mathbf{f}_{\mathbb{U}}^{\text{int}}}{\partial \bar{\mathbb{P}}} \\ \dfrac{1}{\beta \Delta t^2}\mathbf{C} + \dfrac{\gamma}{\beta \Delta t}\mathbf{Q}^T - \dfrac{\partial \mathbf{q}_{\mathbb{P}}^{\text{int}}}{\partial \bar{\mathbb{U}}} & \mathbf{H} + \dfrac{1}{\theta \Delta t}\mathbf{S} - \dfrac{\partial \mathbf{q}_{\mathbb{P}}^{\text{int}}}{\partial \bar{\mathbb{P}}} \end{matrix}\right] \tag{36}
$$

In Eq. (36), the Jacobian matrix needs to be evaluated at each iteration i of time step $\Delta t = t_{n+1} - t_n$. In fact, at each time step a linearized system of equations is solved until the iteration convergence is achieved. Furthermore, it can be seen from (36) that the Jacobian matrix is a non-symmetric matrix, so it is advantageous to make the Jacobian matrix symmetric to save the core

storage and computational cost. For this purpose, the first row of the Jacobian matrix are multiplied by the scalar value $-\gamma/\beta \Delta t$. In addition, the inertial matrices $\mathbf{C}_{\delta\beta}$ are omitted from the Jacobian matrix since the contribution of dynamic seepage forcing terms to the solution is negligible compared to the other terms.

Moreover, it can be seen form (29) that $\mathbf{f}_u^{\text{int}} = 0$ since $[\![\mathbf{N}_u^{std}]\!] = 0$, as a result the derivatives of $\mathbf{f}_u^{\text{int}}$ with respect to the standard and enriched pressure variables are zero, i.e. $\partial \mathbf{f}_u^{\text{int}}/\partial \bar{\mathbf{p}} = 0$ and $\partial \mathbf{f}_u^{\text{int}}/\partial \bar{\mathbf{c}} = 0$. In addition, it can be obtained from (29) that

$$
\frac{\partial \mathbf{f}_{\mathbb{U}}^{\text{int}}}{\partial \bar{\mathbb{U}}} = \left[\begin{matrix} \dfrac{\partial \mathbf{f}_u^{\text{int}}}{\partial \bar{\mathbf{u}}} & \dfrac{\partial \mathbf{f}_u^{\text{int}}}{\partial \bar{\mathbf{a}}} & \dfrac{\partial \mathbf{f}_u^{\text{int}}}{\partial \bar{\mathbf{b}}} \\ \dfrac{\partial \mathbf{f}_a^{\text{int}}}{\partial \bar{\mathbf{u}}} & \dfrac{\partial \mathbf{f}_a^{\text{int}}}{\partial \bar{\mathbf{a}}} & \dfrac{\partial \mathbf{f}_a^{\text{int}}}{\partial \bar{\mathbf{b}}} \\ \dfrac{\partial \mathbf{f}_b^{\text{int}}}{\partial \bar{\mathbf{u}}} & \dfrac{\partial \mathbf{f}_b^{\text{int}}}{\partial \bar{\mathbf{a}}} & \dfrac{\partial \mathbf{f}_b^{\text{int}}}{\partial \bar{\mathbf{b}}} \end{matrix}\right] = 0 \tag{37}
$$

Hence, in order to make the Jacobian matrix symmetric the derivatives of interfacial flux vectors, i.e. $\partial \mathbf{q}_p^{\text{int}}/\partial \bar{\mathbf{u}}$ and $\partial \mathbf{q}_c^{\text{int}}/\partial \bar{\mathbf{u}}$, are eliminated from the first column of the Jacobian matrix. Also, to retain the symmetry of the Jacobian matrix, it is assumed that $\partial \mathbf{f}_{\mathbb{U}}^{\text{int}}/\partial \bar{\mathbb{P}} = \frac{\beta \Delta t}{\gamma}\left(\partial \mathbf{q}_{\mathbb{P}}^{\text{int}}/\partial \bar{\mathbb{U}}\right)^T$, i.e.

$$
\left[\begin{matrix} \dfrac{\partial \mathbf{f}_u^{\text{int}}}{\partial \bar{\mathbf{p}}} & \dfrac{\partial \mathbf{f}_u^{\text{int}}}{\partial \bar{\mathbf{c}}} \\ \dfrac{\partial \mathbf{f}_a^{\text{int}}}{\partial \bar{\mathbf{p}}} & \dfrac{\partial \mathbf{f}_a^{\text{int}}}{\partial \bar{\mathbf{c}}} \\ \dfrac{\partial \mathbf{f}_b^{\text{int}}}{\partial \bar{\mathbf{p}}} & \dfrac{\partial \mathbf{f}_b^{\text{int}}}{\partial \bar{\mathbf{c}}} \end{matrix}\right] = \frac{\beta \Delta t}{\gamma}\left[\begin{matrix} \dfrac{\partial \mathbf{q}_p^{\text{int}}}{\partial \bar{\mathbf{u}}} & \dfrac{\partial \mathbf{q}_p^{\text{int}}}{\partial \bar{\mathbf{a}}} & \dfrac{\partial \mathbf{q}_p^{\text{int}}}{\partial \bar{\mathbf{b}}} \\ \dfrac{\partial \mathbf{q}_c^{\text{int}}}{\partial \bar{\mathbf{u}}} & \dfrac{\partial \mathbf{q}_c^{\text{int}}}{\partial \bar{\mathbf{a}}} & \dfrac{\partial \mathbf{q}_c^{\text{int}}}{\partial \bar{\mathbf{b}}} \end{matrix}\right]^T \tag{38a}
$$

where

$$
\frac{\partial \mathbf{f}_{\alpha}^{\text{int}}}{\partial \bar{\mathbf{p}}_{\delta}} = -\int_{\Gamma_d} [\![\mathbf{N}_u^{\alpha}]\!]^T \mathbf{n}_{\Gamma_d}\mathbf{N}_p^{\delta}d\Gamma \tag{38b}
$$

In addition, it is assumed that $\partial \mathbf{q}_c^{\text{int}}/\partial \bar{\mathbf{p}} = \left(\partial \mathbf{q}_p^{\text{int}}/\partial \bar{\mathbf{c}}\right)^T$, thus

$$
\frac{\partial \mathbf{q}_{\mathbb{P}}^{\text{int}}}{\partial \bar{\mathbb{P}}} = \left[\begin{matrix} \dfrac{\partial \mathbf{q}_p^{\text{int}}}{\partial \bar{\mathbf{p}}} & \dfrac{\partial \mathbf{q}_p^{\text{int}}}{\partial \bar{\mathbf{c}}} \\ \left(\dfrac{\partial \mathbf{q}_c^{\text{int}}}{\partial \bar{\mathbf{p}}}\right)^T & \dfrac{\partial \mathbf{q}_c^{\text{int}}}{\partial \bar{\mathbf{c}}} \end{matrix}\right] \tag{39a}
$$

where

$$
\frac{\partial \mathbf{q}_{\delta}^{\text{int}}}{\partial \bar{\mathbf{p}}_{\gamma}} = -\int_{\Gamma_d}\left(\nabla \mathbf{N}_p^{\delta}\right)^T \cdot \mathbf{t}_{\Gamma_d}k_{fd}(2h)\mathbf{t}_{\Gamma_d}^T \cdot \nabla \mathbf{N}_p^{\gamma}d\Gamma
$$
$$
- \frac{1}{\theta \Delta t}\int_{\Gamma_d}\left(\mathbf{N}_p^{\delta}\right)^T(2h)\frac{1}{K_f}\mathbf{N}_p^{\gamma}d\Gamma \tag{39b}
$$

Based on the above-mentioned simplifications, a symmetric Jacobian matrix can be obtained as

$$\mathbf{J} = \begin{bmatrix} -\frac{\gamma}{\beta \Delta t}\left(\frac{1}{\beta \Delta t^2}\mathbf{M}_{uu} + \mathbf{K}_{uu}\right) & -\frac{\gamma}{\beta \Delta t}\left(\frac{1}{\beta \Delta t^2}\mathbf{M}_{ua} + \mathbf{K}_{ua}\right) & -\frac{\gamma}{\beta \Delta t}\left(\frac{1}{\beta \Delta t^2}\mathbf{M}_{ub} + \mathbf{K}_{ub}\right) & \frac{\gamma}{\beta \Delta t}\mathbf{Q}_{up} & \frac{\gamma}{\beta \Delta t}\mathbf{Q}_{uc} \\ -\frac{\gamma}{\beta \Delta t}\left(\frac{1}{\beta \Delta t^2}\mathbf{M}_{au} + \mathbf{K}_{au}\right) & -\frac{\gamma}{\beta \Delta t}\left(\frac{1}{\beta \Delta t^2}\mathbf{M}_{aa} + \mathbf{K}_{aa}\right) & -\frac{\gamma}{\beta \Delta t}\left(\frac{1}{\beta \Delta t^2}\mathbf{M}_{ab} + \mathbf{K}_{ab}\right) & \frac{\gamma}{\beta \Delta t}\left(\mathbf{Q}_{ap} - \frac{\partial \mathbf{f}_a^{\text{int}}}{\partial \bar{\mathbf{p}}}\right) & \frac{\gamma}{\beta \Delta t}\left(\mathbf{Q}_{ac} - \frac{\partial \mathbf{f}_a^{\text{int}}}{\partial \bar{\mathbf{c}}}\right) \\ -\frac{\gamma}{\beta \Delta t}\left(\frac{1}{\beta \Delta t^2}\mathbf{M}_{bu} + \mathbf{K}_{bu}\right) & -\frac{\gamma}{\beta \Delta t}\left(\frac{1}{\beta \Delta t^2}\mathbf{M}_{ba} + \mathbf{K}_{ba}\right) & -\frac{\gamma}{\beta \Delta t}\left(\frac{1}{\beta \Delta t^2}\mathbf{M}_{bb} + \mathbf{K}_{bb}\right) & \frac{\gamma}{\beta \Delta t}\left(\mathbf{Q}_{bp} - \frac{\partial \mathbf{f}_b^{\text{int}}}{\partial \bar{\mathbf{p}}}\right) & \frac{\gamma}{\beta \Delta t}\left(\mathbf{Q}_{bc} - \frac{\partial \mathbf{f}_b^{\text{int}}}{\partial \bar{\mathbf{c}}}\right) \\ \frac{\gamma}{\beta \Delta t}\mathbf{Q}_{pu}^T & \frac{\gamma}{\beta \Delta t}\left(\mathbf{Q}_{pa}^T - \frac{\partial \mathbf{f}_a^{\text{int}}}{\partial \bar{\mathbf{p}}}\right)^T & \frac{\gamma}{\beta \Delta t}\left(\mathbf{Q}_{pb}^T - \frac{\partial \mathbf{f}_b^{\text{int}}}{\partial \bar{\mathbf{p}}}\right)^T & \mathbf{H}_{pp} + \frac{1}{\theta \Delta t}\mathbf{S}_{pp} - \frac{\partial \mathbf{q}_p^{\text{int}}}{\partial \bar{\mathbf{p}}} & \mathbf{H}_{pc} + \frac{1}{\theta \Delta t}\mathbf{S}_{pc} - \frac{\partial \mathbf{q}_p^{\text{int}}}{\partial \bar{\mathbf{c}}} \\ \frac{\gamma}{\beta \Delta t}\mathbf{Q}_{cu}^T & \frac{\gamma}{\beta \Delta t}\left(\mathbf{Q}_{ca}^T - \frac{\partial \mathbf{f}_a^{\text{int}}}{\partial \bar{\mathbf{c}}}\right)^T & \frac{\gamma}{\beta \Delta t}\left(\mathbf{Q}_{cb}^T - \frac{\partial \mathbf{f}_b^{\text{int}}}{\partial \bar{\mathbf{c}}}\right)^T & \mathbf{H}_{cp} + \frac{1}{\theta \Delta t}\mathbf{S}_{cp} - \left(\frac{\partial \mathbf{q}_p^{\text{int}}}{\partial \bar{\mathbf{c}}}\right)^T & \mathbf{H}_{cc} + \frac{1}{\theta \Delta t}\mathbf{S}_{cc} - \frac{\partial \mathbf{q}_c^{\text{int}}}{\partial \bar{\mathbf{c}}} \end{bmatrix}$$

$$(40)$$

4.4 Numerical integration algorithm

From the computational aspect, one main difficulty encountered when implementing the X-FEM deals with the numerical integration in the presence of the weak or strong discontinuity. In the conventional finite element method, the standard shape functions are in terms of the polynomial order and the Gauss integration rule can be used efficiently to evaluate the integral terms. However, in the extended finite element method the enhanced shape functions are not smooth over an enriched element due to the presence of weak or strong discontinuity inside of the element. Hence, the standard Gauss quadrature rule cannot be used if the element is crossed by a discontinuity, and the discontinuous nature of the solution requires a special treatment to accurately integrate the non-smooth enrichment functions appearing in the enriched part of the X-FEM approximation. In order to carry out the numerical integration in X-FEM, a primary approach is to increase the number of Gauss integration points, as shown in Fig. 4a, however this approach may result in a substantial loss of accuracy. To overcome this difficulty, two techniques are introduced for the numerical integration of an enriched element; the triangular-partitioning method and the rectangular sub-girds method.
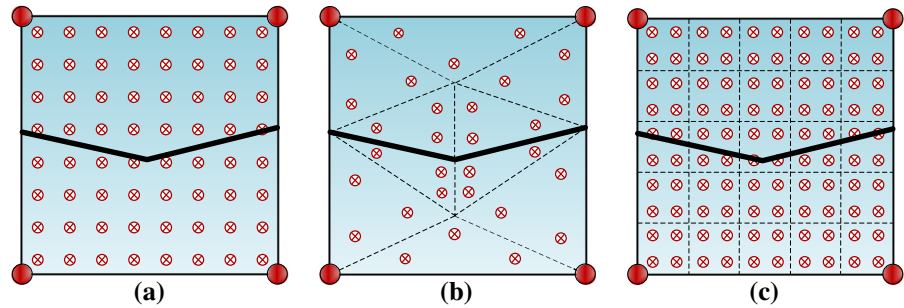
In the triangular-partitioning method, the element bisected by the interface, is divided into sub-triangles, as shown in Fig. 4b, and the Gauss integration rule is performed over each sub-triangle. In this technique, the numerical integration of elements bisected by the discontinuity is performed separately on each sub-element into which the element is divided. In practice, in order to be able to perform the integration over these sub-elements on either side of the discontinuity, each sub-element is partitioned into triangles over which the standard Gauss quadrature is applied. The remaining elements which are not cut by the discontinuity are integrated using the conventional Gauss quadrature scheme. Moreover, a number of Gauss points must be set along the one-dimensional segments of the discontinuity delimited with the element edges to integrate the mechanical and mass transfer coupling terms along the discontinuity.

In an alternative technique, the element cut by the interface is divided into rectangular sub-girds, as shown in Fig. 4c. In this technique, it is not necessary to conform the sub-quadrilaterals to the geometry of interface, however—it is needed to have enough sub-divisions to reduce the error of numerical integration. Based on the rectangular sub-girds integration, the natural coordinates of Gauss quadrature points are independent at each sub-quadrilateral. It must be noted that since the interface does not coincide with the rectangular edges, it may cause some approximation in the numerical simulation; as a result, an accurate solution can be achieved by increasing the number of sub-quadrilaterals.

Although both techniques are quite accurate and are widely used in the extended finite element framework, they each have their own advantages and disadvantages. In the triangular-partitioning method, the integration could be much more accurate since the domain is divided into smooth sub-domains, however—it would be quite cumbersome to develop partitioning for various configurations of interface. Moreover, the possibility of updating the interface due its evolution in time, particularly due to crack propagation, may cause the position of Gauss points to vary during the solution, and as a result it leads to the need for data transferring between the old and new Gauss points. On the contrary in the rectangular sub-grids approach, the data transfer is not necessary as the sub-grids are independent from the configuration of the interface. It is manifest that the

Fig. 4 Numerical integration of an enriched element; **a** the standard Gauss integration points, **b** the triangular-partitioning method, **c** the rectangular sub-girds method

implementation of rectangular sub-gird integration is much easier than the triangular-partitioning algorithm, however—the accuracy cannot be guaranteed in those rectangular sub-girds which is cut by the interface. In order to avoid the inaccuracy involved in this method, the finer sub-girds can commonly be utilized to confine this event. Practically, it is observed that the rectangular sub-grids scheme result in an adequate accuracy.

5 Alternative approaches for fluid flow simulation within the fracture

In preceding sections, the fluid flow within the fracture was modeled by discretizing the flow continuity equation of fluid inside the fracture. For this purpose, the hydro-mechanical coupling associated with the tractions acting on the crack edges and the fluid leak-off from the fracture into the domain was obtained by discretizing the weak form of flow continuity equation of fluid flow inside the fracture in order to compute the interfacial force vector $\mathbf{f}_\alpha^{\text{int}}$ due to the fluid pressure exerted on the fracture faces and the flux vectors q_δ^{int} due to the fluid exchange between the fracture and the surrounding permeable porous medium in Eq. (26). There are basically various techniques proposed by researchers in literature to simulate the fluid flow through the fracture with simplified computational algorithms. These approaches are generally employed for modeling the hydraulic fracturing through impermeable porous media, in which the fluid pressure behaves as an interfacial force on the fracture faces with no direct affect on the fluid pressure of the porous medium surrounding the fracture. These simplifications are mostly valid for rapid crack propagation in an impermeable porous media, and widely used in hydraulic fracturing, which is known as the displacement discontinuity method (Dong and Pater

2001; Akulich and Zvyagin 2008; Zhang and Ghassemi 2011). In this study, two alternative computational algorithms are employed to compute the interfacial forces due to fluid pressure exerted on the fracture faces based on a 'partitioned solution algorithm' and a 'time-dependent constant pressure algorithm' that are mostly applicable to impermeable media, and the results are compared with the coupling X-FEM model described in Sect. 4.

5.1 A partitioned solution algorithm for interfacial pressure

A procedure for numerical approximation of hydraulically driven fracture propagation in a poroelastic material was proposed by Boone and Ingraffea (1990). The method was based on a partitioned solution procedure used to solve the finite element approximation of poroelasticity equations in conjunction with a finite difference approximation for modeling the fluid flow along the fracture. In this method, several assumptions were incorporated in the numerical procedure; firstly the crack-tip is assumed to close smoothly that is a distinctive feature of the Dugdale–Barenblatt fracture model, secondly there is a coupling between the fluid flow in the fracture and the surrounding porous medium, and finally the fluid flow along the fracture does not reach the crack-tip so a region may exist near the crack-tip which is void of fluid.

In this study, the partitioned solution procedure proposed by Boone and Ingraffea (1990) is employed as an alternative solution to compute the fluid pressure exerted on the fracture faces of an impermeable porous media. In this simplified method, it is assumed that the flow is laminar, the fluid is incompressible, and it accounts for the time-dependent rate of crack opening. Hence, the fluid mass conservation equation can be stated as

$$\frac{\partial q}{\partial \bar{x}} - \frac{\partial w}{\partial t} + q_1 = 0 \tag{41}$$

where w is the fracture opening ($w = 2h$), and q_1 is the fluid leak-off into the surrounding porous medium, which is equal to zero for the case of impermeable porous media. In the above equation, q is the flow rate along the fracture length $\bar{x}$ defined as

$$q = -\frac{w^3}{12\mu_f}\frac{\partial p}{\partial \bar{x}} \tag{42}$$

where μ_f is the viscosity of fluid within the fracture and p is the fluid pressure along the fracture. It must be noted that this approach can be used for the case of permeable porous medium by employing some experimental relations for the fluid leak-off q_1.

In order to solve the fluid mass conservation Eq. (41), the finite difference algorithm is employed using a predetermined value of fracture length, where the fracture is in equilibrium between the in situ stress and the pressure distribution in the fracture. The crack interface allows the fracture to open when subjected to an internal pressure. A control-volume approach is proposed to model the fluid flow within the fracture. Basically, an iterative procedure is used to solve for the length and opening of the crack. For this purpose, a number of control points are determined along the crack interface and Eq. (41) is satisfied for each control point. The set of equilibrium equations are finally solved over all control points along the crack interface, as shown in the flow-chart of Fig. 5a. In this algorithm, the crack opening w is obtained from the X-FEM solution so that the unknown value from Eq. (41) is the fluid pressure p. Assembling the set of equations for the individual control volumes constructed over the control point results in a tridiagonal matrix. This fluid flow model is first constructed for the complete length of the predetermined fracture path. The control volumes are given a nominal, small initial width so that the equations are well-posed. The boundary conditions for each time step are specified as a fixed pressure at the crack mouth and zero flow at the other end of the fracture. The fluid within the fracture is assumed to be incompressible so that there can be no flow past the tip of the fracture, even though the zero-flow condition is imposed at the end of the row of control volumes. Generally, it would be desirable to be able to impose a flow rate as a boundary condition at the crack mouth. However, the imposition of a Neumann boundary condition as the crack mouth pressure results in an ill-posed set of equations. In order to impose this
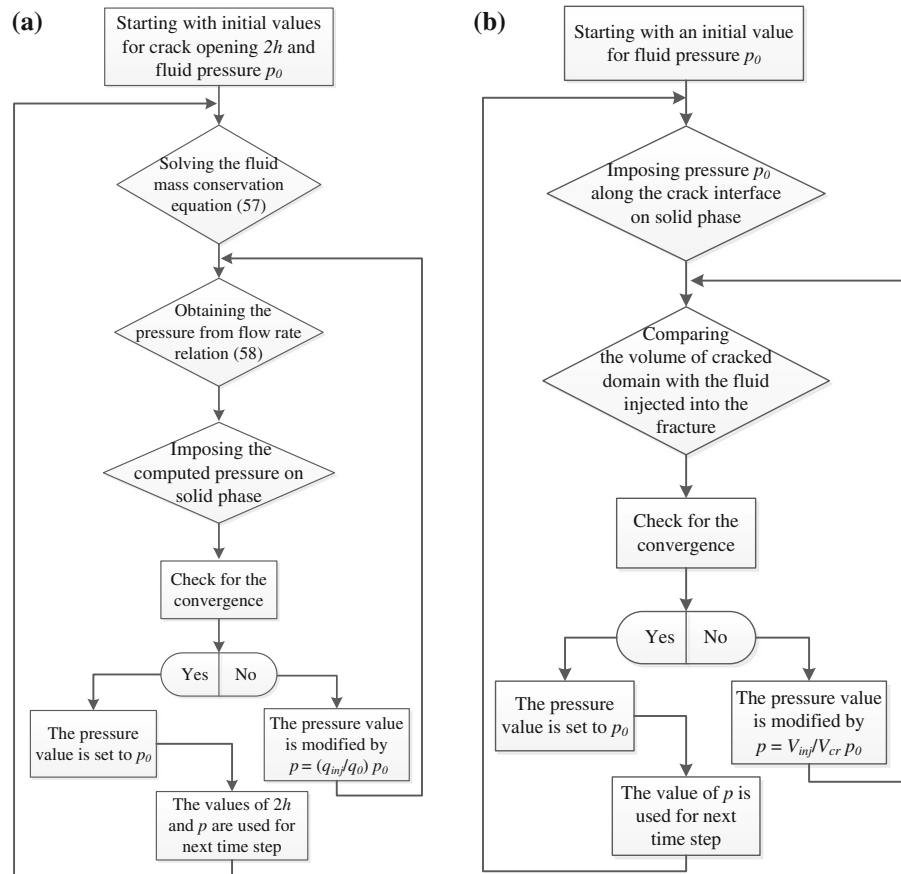
boundary condition in conjunction with the partitioned analysis procedure, it is necessary to impose a pressure boundary condition elsewhere along the fracture. However, the pressure along the fracture is not known and it cannot be imposed at the crack-tip owing to the existence of a singularity in the pressure at this point.

It must be noted that there must be a one-to-one correspondence between the control volumes and the elements bisected by the crack along the fracture interface in the X-FEM solution. This ensures that fluid mass is conserved across the boundary. Basically, two situations may occur for coupling along the fracture depending on whether the fracture faces are assumed permeable, or impermeable. For impermeable faces, the fluid pressures in the fracture are converted to equivalent external loads on the fracture faces. For permeable faces, the fluid pressure in the fracture must be applied as a pore pressure and a total stress boundary condition. It is also necessary to obtain a solution where the fluid leak-off from the fracture is consistent with the flow across the interface in the X-FEM solution. It must be noted that the proposed finite difference algorithm is not unconditionally stable and the convergence can be generally achieved using a large number of iterations.

5.2 A time-dependent constant pressure algorithm

In hydraulic fracturing, an essential ingredient in establishing a formulation for hydraulically driven fracture propagating in the porous medium is to perform a relationship between the injection rate, fluid leak-off, fracture width, fracture length, and the total volume pumped into the formation. This formulation was comprehensively derived in Sect. 4 by discretizing the continuity equation of fluid flow inside the fracture in the framework of X-FEM formulation and evaluating the tractions acting on the crack edges and the fluid leak-off from the fracture into the porous medium based on Eqs. (29) and (30). An alternative technique was proposed in the previous section on the basis of a 'partitioned solution algorithm' in the framework of finite difference method by satisfying the fluid mass conservation equation over a number of control points along the fracture interface. Although the method was presented for the case of impermeable porous media, it can easily be extended to the permeable porous media using some experimental relations for the fluid leak-off behavior. In this section, a simplified approach is presented based

Fig. 5 The flowchart of the solution; **a** the 'partitioned solution algorithm', **b** the 'time-dependent constant pressure algorithm'

(a)

Starting with initial values for crack opening *2h* and fluid pressure p_0

Solving the fluid mass conservation equation (57)

Obtaining the pressure from flow rate relation (58)

Imposing the computed pressure on solid phase

Check for the convergence

Yes | No

The pressure value is set to p_0

The pressure value is modified by $p = (q_{inj}/q_0)\, p_0$

The values of *2h* and *p* are used for next time step

(b)

Starting with an initial value for fluid pressure p_0

Imposing pressure p_0 along the crack interface on solid phase

Comparing the volume of cracked domain with the fluid injected into the fracture

Check for the convergence

Yes | No

The pressure value is set to p_0

The pressure value is modified by $p = V_{inj}/V_{cr}\, p_0$

The value of *p* is used for next time step

on a 'time-dependent constant pressure algorithm' to evaluate the traction forces acting on the fracture edges for the case of impermeable porous media.

It has been observed from the solution of hydraulic fracturing in porous media that the pressure distribution in the fracture is almost constant along the crack interface. Geertsma and Klerk (1969) developed a method based on the concept of equilibrium fracture propagation, and derived a simplified pressure distribution in the direction of fracture propagation. An analytical solution was obtained by Spence and Sharp (1985), in which the internal flow was modeled by lubrication theory that results in a nonlinear partial differential equation connecting the pressure to the cavity shape, and the solution was studied for a special case of the constant pressure distribution. Detournay (2004) investigated the propagation regimes of fluid-driven fractures in impermeable rocks, where a limit of zero viscosity was considered in order to develop a dimensionless variable for the solution. The idea of constant pressure distribution along the fracture for the case of imper-

meable porous media has been widely used in various numerical implementation of hydraulic fracturing due to its simplicity. It must be noted that the only measurable quantities that are directly related to the fracture propagation process are the total volume of fluid injected into the fractured domain and the time to accomplish this process. Moreover, considering the case of no leak-off of fracture fluid into the surrounding porous medium, it implies that all fluid injected into the fracture must be used to propagate the fracture, both in the width and the length.

In this study, the idea of constant pressure distribution along the crack is modified to be able to model the propagation of fluid-driven fracture in time. In fact, the modification is performed because of some limitations on the 'partitioned solution algorithm' discussed in previous section, due to imposition of the Neumann boundary condition as a flow rate at the crack mouth and the low convergence rate of the solution. Basically, two types of boundary conditions can be employed in hydraulic fracturing problems; the crack mouth pres-

sure as an essential boundary condition, in which no modification is needed and the imposed pressure can be used everywhere along the fracture during the solution; and the flow rate at the crack mouth as a natural boundary condition, in which an auxiliary assumption is used to solve the fluid mass conservation Eq. (41). By injecting the fluid flow into the fracture with no leak-off into the surrounding porous medium, the volume of cracked domain must be equal to the total volume of fluid injected into the fractured zone. This results in a decrease of the fluid pressure through the time as the crack propagates and reaches almost a steady value when the crack-tip proceeds far away from the injection point, as has been already observed in hydraulic fracturing problems. It must be noted that the fluid flow is assumed to be incompressible since the volume change is negligible in the simulation of hydraulic fracturing problem proposed here. The flowchart of the solution is presented in Fig. 5b for the 'time-dependent constant pressure algorithm'. The computational algorithm starts with an initial value of pressure along the fracture for each time step; the value of fracture opening is then obtained from the X-FEM solution by imposing the predetermined pressure on the fracture faces of the porous medium as external tractions; the solution follows by comparing the volume of cracked domain with the total volume of fluid injected into the fractured zone; the value of pressure is then modified based on the ratio of the volume of cracked domain to the volume of fluid injected into the domain. The process continues until the convergence is achieved. It has been shown through the numerical simulation results that the proposed technique results in a reasonable accuracy and a great numerical stability; the number of iterations and the rate of convergence are quite satisfying proving the soundness of proposed computational algorithm.

6 Crack growth simulation

The crack growth simulation is one of the most cumbersome tasks in the finite element framework. In the standard FEM method, since the crack evolves through the finite element mesh, the solution algorithm must be updated at each crack growth by modifying the FE mesh in new configuration. However, in the extended finite element modeling, the crack geometry is modeled independent of the finite element mesh by enriching the nodal points of elements that are intersected by the crack during crack propagation. In crack growth simulation, the crack propagates with a predefined value of crack length, if the crack propagation criterion is satisfied. In the X-FEM, the Heaviside and crack-tip enrichments are used according to the current position of the crack-tip at each time step. Based on these enrichments, the simulation is performed to obtain the stress and displacement fields at the crack-tip region, in order to indicate the crack-tip position in the next step of crack growth. If the new crack-tip position is in the area of former element, no update is necessary for the enriched elements; however, if the new crack segment crosses the next element, the enrichment of nodal points must be updated. The simulation can then be carried out according to the new enriched elements based on the new configuration of crack propagation. It must be noted that this method needs a high accurate recognition function to diagnose the position of new crack-tip elements.

In crack propagation problems, there are two main requirements at each time step. It must be first determined whether the crack propagates or not; and if so in which direction the crack propagates. Based on these two requirements, two criteria must be utilized; one for crack propagation and the other for crack kinking. In this study, two different enrichment strategies are employed for crack growth simulation, as described in the section of numerical simulation results. In the first case, the asymptotic enrichment functions are employed at the crack-tip element to model the singularity at the tip of discontinuity, the Heaviside enrichment function to model the displacement jump across the fracture, and the modified level-set function to model the discontinuity on the gradient of fluid pressure normal to the fracture. While in the second case, the crack-tip enrichment functions are removed from the X-FEM simulation, and the Heaviside enrichment function and the modified level-set function are used only to model the displacement and pressure fields, respectively.

In order to model the crack propagation in the framework of linear fracture mechanics, a criterion can be defined based on a function of the stress intensity factors, the strain energy release rate, the strain energy density and etc. The crack kinking criteria determines the direction of the crack and can be determined based on the fracture toughness of brittle material, which is usually measured in a pure mode I loading conditions noted by K_{IC}. For a general mixed mode case,

a criterion is needed to determine the angle of incipient propagation with respect to crack direction, and a critical combination of stress intensity factors that leads to crack propagation. There are various criteria which have been proposed by researchers for the mixed mode crack propagation, including the maximum energy release rate, the minimum strain energy density criteria, the maximum circumferential tensile stress and etc. In this study, the maximum circumferential tensile stress is employed, where the hoop stress reaches its maximum value on the plane of zero shear stress. The crack propagation angle θ_0 is expressed by using the angle between the line of crack and the crack growth direction, with the positive value defined in the anti-clockwise direction, as

$$\theta_0 = 2\arctan\left(\frac{K_I}{4K_{II}} \pm \frac{1}{4}\sqrt{\left(\frac{K_I}{K_{II}}\right)^2 + 8}\right) \qquad (43)$$

in which the sign is chosen such that the hoop stress is positive. To initiate crack propagation, it needs that the maximum circumferential tensile stress σ_θ reaches a critical value. However, when the plastic zone size cannot be ignored, it is necessary to use the stress state at a material dependent finite distance from the crack-tip.

In order to perform the crack growth simulation with no crack-tip enrichments, the maximum principal tensile stress is checked at all integration points in the element ahead of the tip of the discontinuity at the end of a load increment. If the maximum principal tensile stress at any of the integration points in the element ahead of the crack-tip reaches the tensile strength of the material, the discontinuity is introduced through the entire element. The discontinuity is inserted as a straight line within the element and is enforced to be geometrically continuous. Note that the crack propagation length is limited here to a single element size, as the time steps are very small and the rate of crack growth is assumed to be quite slow during the simulation. In this model, since a crack propagates from a discrete point, the discontinuity can be handled in two ways, the first by choosing a point before the calculation and the second by performing an elastic loading and checking where the principal stresses are greatest. It must be noted that the discontinuity is extended only at the end of a load increment in order to preserve the quadratic convergence rate of the full Newton–Raphson solution procedure. The most important ingredient when extending a discontinuity is that the correct direction is chosen. Since the tip of the discontinuity is not located at a point where the stress state is known accurately, such as conventional Gauss points, the local stress field cannot be relied upon to accurately yield the correct normal vector to a discontinuity. To overcome this, the averaged stress tensor or the so-called non-local stress tensor is used at the crack-tip to obtain the principal stress direction and to determine the right direction of the discontinuity extension. The discontinuity is extended in the direction perpendicular to the maximum non-local principal stress direction. It must be noted that the jump in the displacement field at the tip of the discontinuity must be equal to zero. In order to enforce this condition, the nodes belonging to the element edge on which the tip of the discontinuity lies are not enriched. Since the enrichment functions are multiplied by the shape functions of a particular node, the enhanced basis at a particular node has an influence only over the support of that node. Therefore, the Heaviside function is added only to the enhanced basis of nodes whose support is crossed by a discontinuity. Another condition that must be satisfied is that the displacement jump at the crack-tip be zero. To ensure this, the nodes on the element boundary touched by the crack-tip are not enhanced. When a discontinuity propagates into the next element, all nodes behind the crack-tip are enhanced.

7 Numerical simulation results

In order to illustrate a part of the wide range of problems that can be solved by the proposed approach and to validate the performance of the computational algorithm in modeling of the hydraulic fracturing problem, several numerical examples are solved. The first example demonstrates the robustness of X-FEM in mixed mode fracture analysis of an infinite saturated porous media with an inclined crack. The numerical simulation is compared with an available numerical modeling reported in literature. The next two examples are chosen to demonstrate the robustness of X-FEM technique in simulation of hydraulically driven fracture propagation in an infinite poroelastic medium and a gravity dam under hydrostatic pressure. The maximum circumferential stress criterion is employed to determine the crack growth direction, and the computational algorithm presented in Sect. 4 is performed to obtain the crack trajectory at different load steps for these complex geometries. It must be noted that a

Fig. 6 An infinite saturated porous medium with an inclined crack; Problem definition and the X-FEM meshes
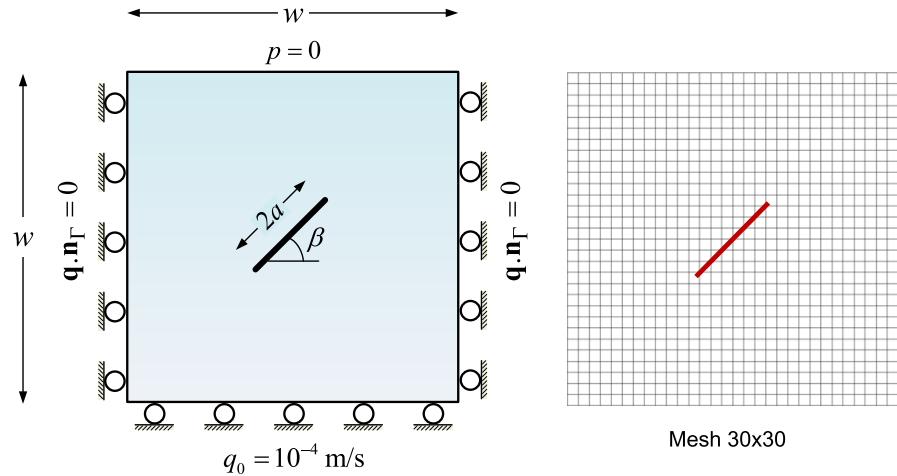
Table 1 Material properties of an infinite saturated porous medium with an inclined crack

Young modulus	$E = 9\,\mathrm{GPa}$
Poisson ratio	$\nu = 0.4$
Biot constant	$\alpha = 1$
Porosity	$n = 0.3$
Solid phase density	$\rho_s = 2{,}000\ \mathrm{kg/m^3}$
Water density	$\rho_w = 1{,}000\ \mathrm{kg/m^3}$
Bulk modulus of solid phase	$K_s = 1.0 \times 10^{27}\ \mathrm{GPa}$
Bulk modulus of water	$K_w = 1.0 \times 10^{27}\ \mathrm{GPa}$
Permeability	$k = 1.0 \times 10^{-9}\ \mathrm{m^3/Ns}$
Viscosity of water	$\mu_w = 1 \times 10^{-3}\ \mathrm{Pas}$

main issue with the coupling finite element formulation of hydro-mechanical simulation is the numerical stability. In such case, it is necessary to investigate the inf-sup condition, called as the LBB condition. A comprehensive study on stabilization strategies in coupled poro-mechanical problems was presented by Preisig and Prevost (2011). Sun et al. (2013) proposed an adaptive stabilized scheme for coupled poro-mechanical problems within the finite strain formulation, which was capable to overcome the locking issue due to shear failure, handling the pore fluid and solid skeleton incompressibility, and satisfying the inf-sup condition simultaneously. In the current study, the oscillations are removed by using a very fine mesh at the region of hydraulic fracturing with the drainage boundary condition. It has been observed that there are not considerable oscillations in the pressure field using the proposed computational approach.

7.1 An infinite saturated porous medium with an inclined crack

The first example is chosen to illustrate the performance of X-FEM model in hydro-mechanical analysis of an inclined crack within an infinite saturated porous media, as shown in Fig. 6. This example was originally proposed by Réthoré et al. (2007b) to present their X-FEM formulation for modeling the fluid flow in a fractured porous medium, and used here for comparison. A square-shaped fractured domain of $10\,\mathrm{m} \times 10\,\mathrm{m}$ with an inclined crack of length 2 m at its center is modeled in a plane strain condition, which is subjected to a normal fluid flux of $q_0 = 10^{-4}$ m/s at the bottom surface while the top surface is imposed as a drained condition. The geometry, boundary conditions and the position of the fault are shown in Fig. 6. The left and right edges are assumed to have an undrained boundary condition. The material properties of the soil are given in Table 1. The X-FEM analysis is performed using a quadrilateral structured FE mesh of 30×30 at different crack angles of $\beta = 15°$, $30°$ and $45°$. The problem is solved for a total period of 10 s in 75 time steps.

In Fig. 7a, the distribution of vertical displacement contour is shown for the fracture angle of $\beta = 30°$ at time step $t = 10$ s. Obviously, the imposed fluid flux at the bottom of the porous medium increases the fluid pressure through the domain and as a result inside the fracture, so the crack opens and the fluid flows inside the fracture. In Fig. 7b, the contour of pressure gradient is shown in the normal direction to the fracture at time step $t = 10$ s. Clearly, a jump can be observed at both tips of the discontinuity. It is obvious that the fluid flows

Fig. 7 An infinite saturated porous medium with an inclined crack at the crack angle of $\beta = 30^{\circ}$; **a** the distribution of vertical displacement contour, and **b** the contour of pressure gradient normal to discontinuity at the time step of $t = 10\,\mathrm{s}$
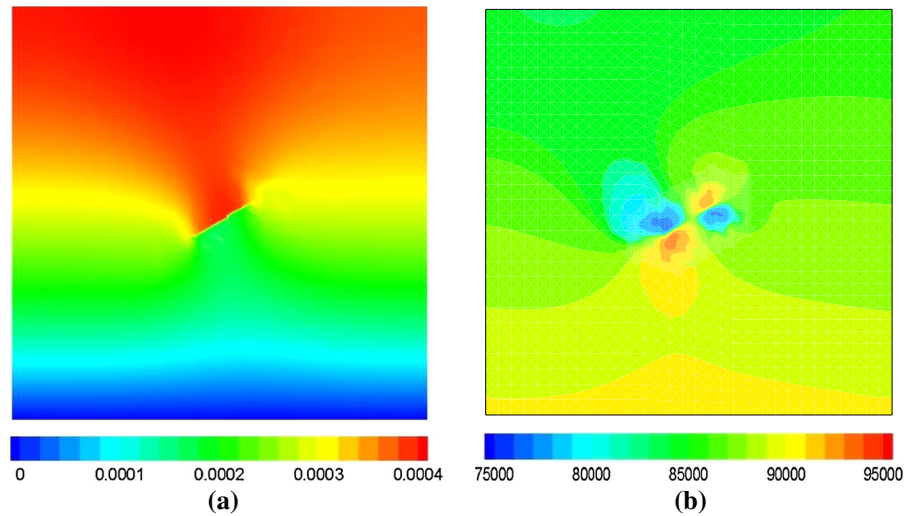
inside the crack from the left crack-tip to the right one because of the imposed fluid flux at the bottom edge. A maximum pressure gradient can be seen at the bottom-left of the crack-tip and a minimum value at the top-left, representing that a considerable amount of fluid flows through the fracture. In contrast, the minimum pressure gradient at the bottom-right and its maximum value at the top-right of the crack-tip cause the flow of fluid from the fracture into the porous medium. In Fig. 8, the evolutions of the ratio of out-flow to in-flow (imposed fluid flux), i.e. q_{out}/q_0, are plotted for different fracture angles, and the results are compared with that obtained without a fracture. It can be clearly observed that the presence of the fracture affects the flow of fluid from the bottom to the top of the domain, described in terms of the ratio of out-flow to in-flow in this figure. In fact, a part of the fluid can be stored inside the fracture that causes the fluid flow to decrease for the lower fracture angle. Similar results were reported by Réthoré et al. (2007b) that demonstrates a good performance of proposed computational algorithm for modeling the fluid flow through a fractured porous medium.

### 7.2 Hydraulic fracture propagation in an infinite poroelastic medium

The next example illustrates the performance of proposed X-FEM model for the simulation of hydraulically driven fracture propagation in an infinite porous media. An analytical solution was obtained for this example by Spence and Sharp (1985) and Emerman
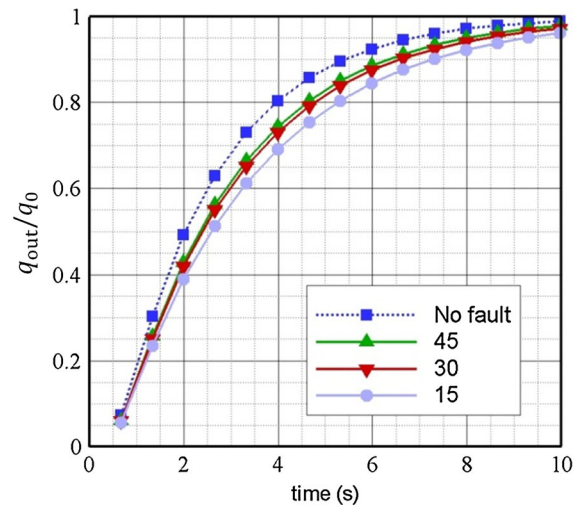
Fig. 8 The ratio of out-flow to in-flow (q_{out}/q_0) for a fractured porous media at different crack angles

et al. (1986) and used here for comparison. The example was also modeled by Boone and Ingraffea (1990) to present their staggered procedure, in which a finite element method was applied for the mechanical problem and a finite difference method for the flow analysis through the fracture. The hydraulic fracturing problem was modeled using the adaptive FEM strategy to study the static and dynamic behavior of fractured domain in saturated porous media (Schrefler et al. 2006; Secchi et al. 2007; Barani et al. 2011; Khoei et al. 2011). In this study, the hydraulic fracture propagation is modeled based on the proposed X-FEM technique to overcome the expensive and cumbersome computational costs

Fig. 9 A hydraulically driven fracture propagation in an infinite porous media. A schematic illustration of the problem, geometry, boundary conditions and X-FEM mesh
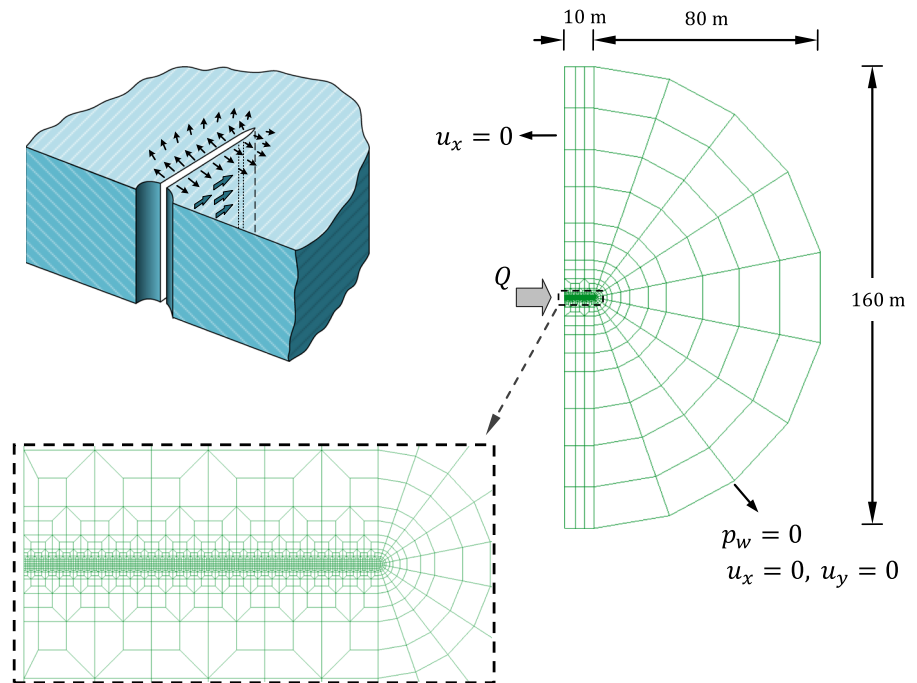
encountered during the mesh generation process in crack growth simulation. The problem is solve using the coupling X-FEM computational algorithm described in Sect. 4, and the results are compared with the simplified computational models of 'partitioned solution algorithm' and a 'time-dependent constant pressure algorithm' described in Sect. 5.

The hydraulic fracture problem demonstrates the injection of fluid into a borehole at the constant rate of Q that causes the fracture to advance into the porous medium. Due to the symmetry of problem, the circular borehole is solved for one-half of the specimen containing a tip, from which the crack enucleates. In Fig. 9, the geometry and boundary condition of problem are presented together with the X-FEM mesh. A finite element mesh of 2,420 quadrilateral elements is employed where the size of elements around the borehole is assumed to be 0.05 m × 0.05 m. The mesh size is fine enough to represent accurately the distribution of the fluid pressure in the direction of the propagating fracture and to guarantee the mesh independence and numerical convergence of the solution. The material properties of poroelastic medium are given in Table 2. An initial crack of length 0.05 m is assumed at the borehole where the fluid injection is imposed, and a constant flow rate of 0.0001 m^2/s is applied at the crack mouth. The crack propagates in the normal direction to

Table 2 Material properties of hydraulic fracture propagation in an infinite poroelastic medium

|	
Shear modulus	$G = 6\,\text{GPa}$
Drained Poisson ratio	$v = 0.2$
Undrained Poisson ratio	$v_u = 0.33$
Biot constant	$\alpha = 1$
Porosity	$n = 0.19$
Solid phase density	$\rho_s = 2,000\,\text{kg/m}^3$
Water density	$\rho_w = 1,000\,\text{kg/m}^3$
Bulk modulus of solid phase	$K_s = 36.0\,\text{GPa}$
Bulk modulus of water	$K_w = 3.0\,\text{GPa}$
Permeability	$k = 6.0 \times 10^{-12}\,\text{m}^3/\text{Ns}$
Viscosity of water	$\mu_w = 1 \times 10^{-3}\,\text{Pas}$
Tensile strength	$\sigma_{ult} = 1\,\text{MPa}$

the maximum principal tensile stress when the principle effective stress at the crack-tip reaches the ultimate tensile strength of the material 1.0 MPa. In order to evaluate the accuracy of proposed computational algorithm, the mass matrix is set to zero. The problem is solved for 10 s with the time increment chosen as 0.01 s to achieve the results independent of the temporal discretization.

In the limiting case where there is no fluid leak-off and under the simplifying assumption that the fracturing fluid is incompressible and the surrounding porous

Table 3 Constants A, B and C given by Geertsma and Klerk (1969) and Spence and Sharp (1985)

Parameter	Spence and Sharp (1985)	Geertsma and Klerk (1969)
A	2.14	1.87
B	1.97	1.38
C	0.65	0.68

Fig. 10 The variations with time of the crack length (CL), crack mouth pressure (CMP), and crack mouth opening displacement (CMOD). A comparison between the coupling X-FEM method, the X-FEM method based on the 'partitioned solution algorithm', the X-FEM method based on the 'time-dependent constant pressure algorithm', and those of analytical solutions
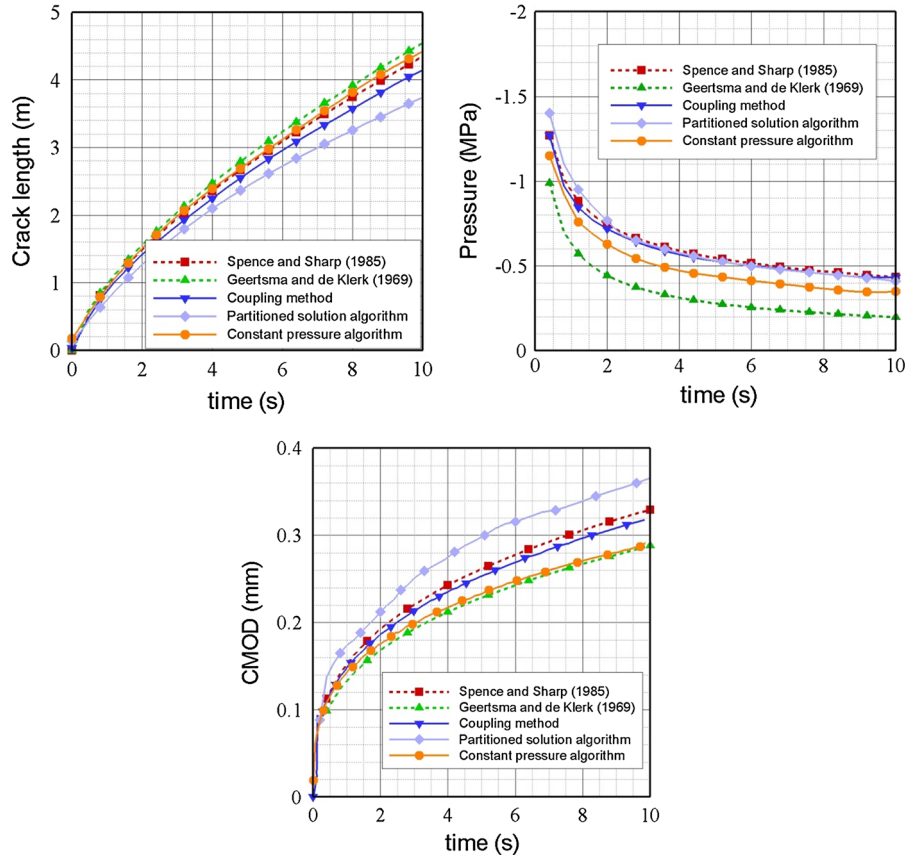
medium is impermeable, the analytical solutions were reported by Geertsma and Klerk (1969) and Spence and Sharp (1985) in terms of the crack mouth opening displacement (CMOD), crack mouth pressure (CMP) and crack length (CL) as

$$\text{CMOD} = A \left(\frac{\mu(1-\nu)Q^3}{G} \right)^{1/6} t^{1/3}$$

$$\text{CMP} = B \left(\frac{G^3 Q\mu}{(1-\nu)^3 L^2} \right)^{1/4} + S$$

$$\text{CL} = C \left(\frac{GQ^3}{\mu(1-\nu)} \right)^{1/6} t^{2/3} \tag{44}$$

where S is the in situ stress normal to the crack growth direction, G is the shear modulus, μ is the fluid vis-

cosity, t is the time, and parameters A, B and C are constants given in Table 3 based on the solutions of Geertsma and Klerk (1969) and Spence and Sharp (1985).

In Fig. 10, the variations with time of the crack length (CL), crack mouth pressure (CMP), and crack mouth opening displacement (CMOD) are plotted using the coupling X-FEM method, the X-FEM method based on the 'partitioned solution algorithm', and the X-FEM method based on the 'time-dependent constant pressure algorithm', and the results are compared with those of analytical solutions reported by Geertsma and Klerk (1969) and Spence and Sharp (1985). Obviously, there is a good agreement between the results of coupling X-FEM method and the analytical solution obtained

by Spence and Sharp (1985). It can be seen that the results of 'time-dependent constant pressure algorithm' are close to those of analytical solution obtained by Geertsma and Klerk (1969), particularly the profiles of the crack length (CL) and crack mouth pressure (CMP). It must be noted that the convergence is achieved in this method with a maximum number of three iterations for each time step. However, the results of 'partitioned solution algorithm' present a noticeable difference from the two analytical solutions, as can be seen from the profiles of the crack length (CL) and crack mouth opening displacement (CMOD). Moreover, a low convergence rate was observed in the solu-

tion of 'partitioned solution algorithm'. Hence, it can be highlighted that the 'time-dependent constant pressure algorithm' proposed here can be considered as an efficient simplified algorithm for the case of impermeable medium. Finally, the contours of vertical displacement, fluid pressure, and maximum principal stress are shown in Fig. 11 at the time step $t = 10$ s for three computational algorithms, i.e. the coupling X-FEM method, the X-FEM method based on the 'partitioned solution algorithm', and the X-FEM method based on the 'time-dependent constant pressure algorithm'. Obviously, the overall performances of all three computational models are acceptable. An important issue inves-
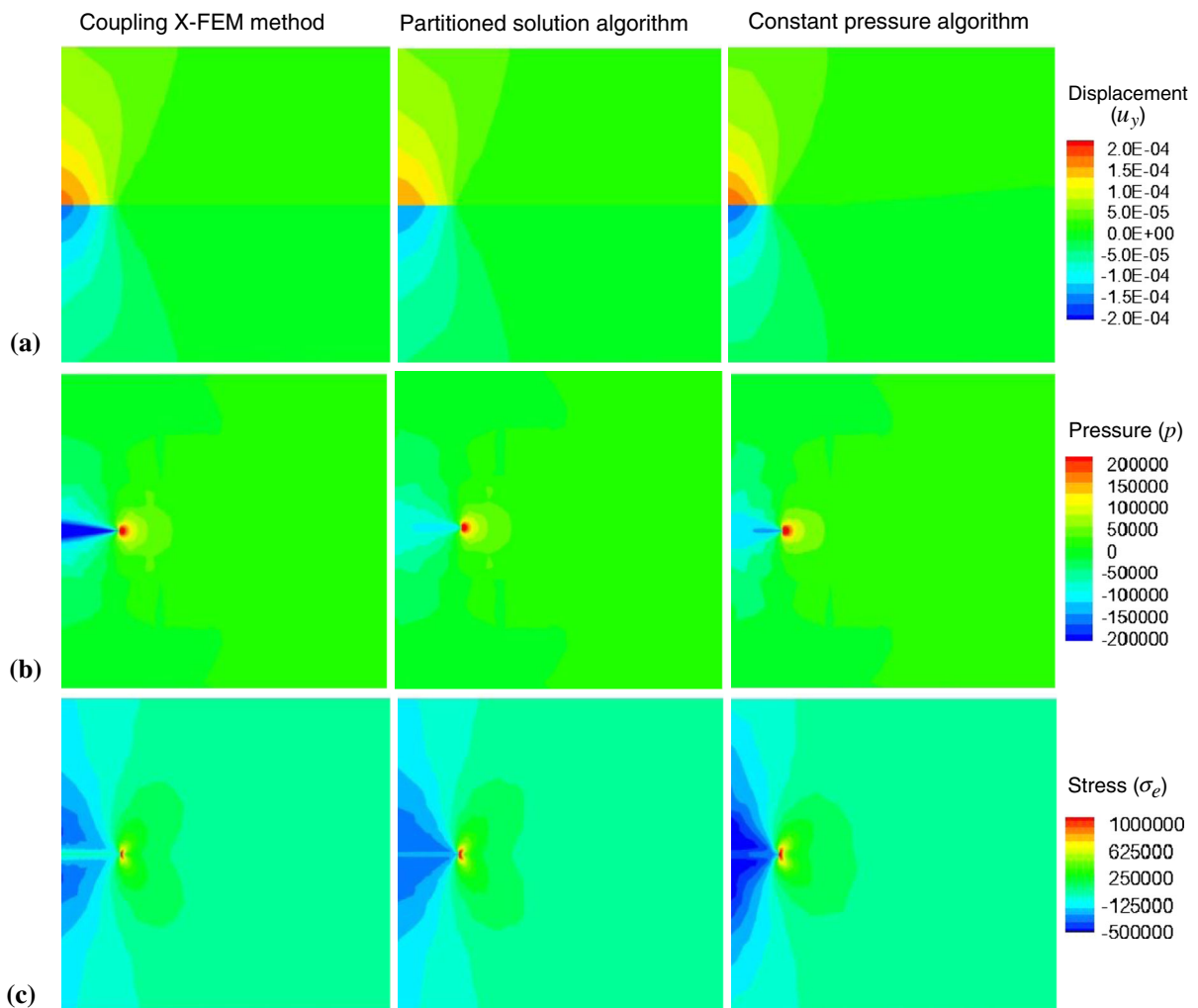
Fig. 11 The contours of **a** vertical displacement, **b** fluid pressure, and **c** maximum principal stress using the coupling X-FEM method, the X-FEM method based on the 'partitioned solution algorithm', and the X-FEM method based on the 'time-dependent constant pressure algorithm'

Table 4 The hydraulic fracture propagation in an infinite poroelastic medium; The residual norms at the first time step

| Iterations	Coupling X-FEM method	Partitioned solution algorithm	Time-dependent constant pressure algorithm
1	1.000E+1	1.000E+1	1.000E+1
2	0.446E−05	0.143E−01	0.283E+0
3	0.558E−10	0.142E−01	0.389E−14
4	0.122E−14	0.142E−01	
⋮		⋮	
21		0.975E−02	
⋮		⋮	
35		0.997E−03	
⋮		⋮	
50		0.870E−04	
⋮		⋮	
64		0.895E−05	
⋮		⋮	
78		0.919E−06	
⋮		⋮	
193		0.719E−14	

tigated in this example is the convergence rate involved in each approach. It was mentioned earlier that the coupling X-FEM method and the X-FEM method based on the 'time-dependent constant pressure algorithm' introduce a great convergence rate during the analysis. However, the X-FEM method based on the 'partitioned solution algorithm' requires a large number of iterations for achieving a desirable norm of convergence. In Table 4, the profiles of convergence rate are given for all three approaches at the first time step of the solution that present a great performance of the coupling X-FEM method and the X-FEM method based on the 'time-dependent constant pressure algorithm'.

7.3 Hydraulic fracturing in a concrete gravity dam

The last example is chosen to illustrate the performance of proposed X-FEM method for a challenging problem of a concrete gravity dam under hydrostatic pressure due to water pressure in the reservoir and the dam self-weight. The dam geometry is similar to the ICOLD benchmark exercise A2 (*Proceedings of 5th ICOLD International Benchmark Workshop on Numer-*

ical Analysis of Dams 1999). This practical example was modeled by Schrefler et al. (2006) using a quasi-static cohesive fracture analysis, and Khoei et al. (2011) using a dynamic analysis of cohesive fracture propagation. In the simulation presented here, the coupling X-FEM method is employed to evaluate the pattern of crack growth in the dam concrete foundation, and the results are compare with the 'constant pressure algorithm'. The geometry, boundary condition and X-FEM mesh are shown in Fig. 12. The material parameters for numerical simulation are given in Table 5. The zero initial pore pressure is assumed for the concrete dam. The problem is solved for the total time of 0.7 s with the time step chosen as 0.002 s. The dam is modeled under the hydrostatic pressure of the reservoir, where the level of water is set to 70 m. The crack is automatically induced in the dam using the maximum tensile effective stress criterion, and propagated in a direction perpendicular to the maximum tensile effective stress.

In Fig. 13, the contours of maximum principal stress are presented at time step $t = 0.7$ s, where the fracture length is equal to 3.5 m using the coupling X-FEM method and the X-FEM method based on the 'constant pressure algorithm'. It must be noted that
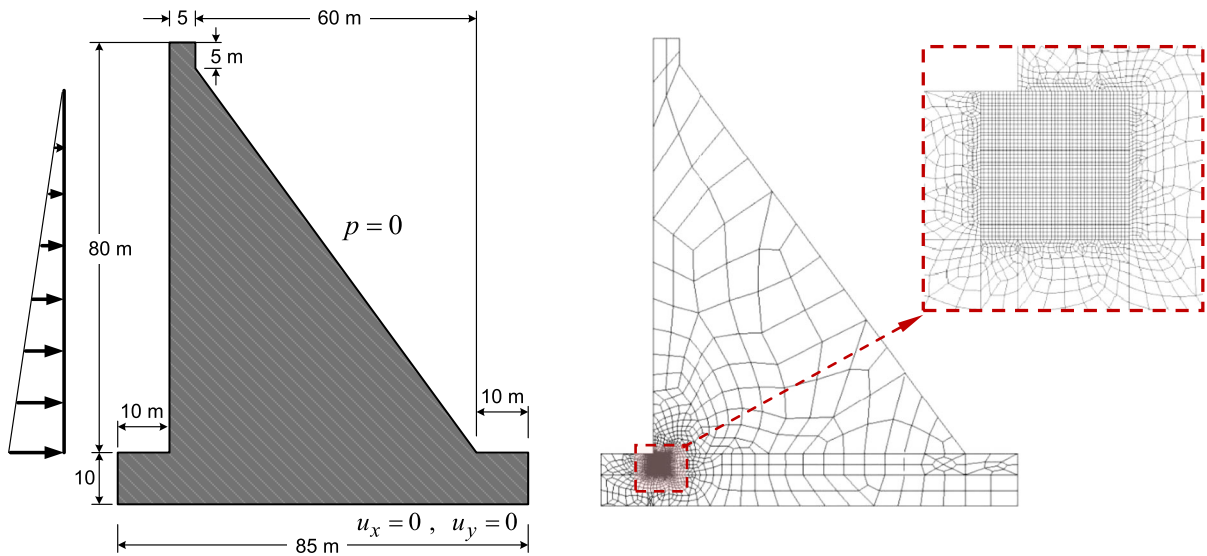
Fig. 12 A concrete gravity dam under hydrostatic pressure; The geometry, boundary condition and X-FEM mesh

Table 5 Material properties of the concrete gravity dam

|	
Elasticity modulus	$E = 24$ GPa
Poisson ratio	$\nu = 0.15$
Biot constant	$\alpha = 1$
porosity	$n = 0.19$
Density	$\rho_s = 2{,}400$ kg/m^3
Water density	$\rho_w = 1{,}000$ kg/m^3
Bulk modulus of solid phase	$K_s = 36.0$ GPa
Bulk modulus of water	$K_w = 3.0$ GPa
Permeability	$k = 10^{-18}$ m^3/Ns
Viscosity of water	$\mu_w = 1 \times 10^{-3}$ Pas
Tensile strength	$\sigma_{ult} = 1.5$ MPa

in the 'constant pressure algorithm' proposed here, a pressure boundary condition is assumed at the crack mouth, so the analysis is carried out using a constant water pressure acting on crack faces along the fracture interface equal to the level of water in the reservoir. Obviously, an almost identical stress contours can be seen between two computational models, which are in a good agreement with those reported by Schrefler et al. (2006) and Khoei et al. (2011) using an adaptive mesh refinement technique. In Fig. 14, the patterns of crack growth in concrete dam are depicted for the coupling X-FEM method and the 'constant pressure algorithm' that show a good agreement with that reported

by Khoei et al. (2011). In Fig. 15, the variations with time of the crack length (CL) and crack mouth opening displacement (CMOD) are plotted for the coupling X-FEM method and the 'constant pressure algorithm', and the results are compared with those reported by Khoei et al. (2011). Clearly, a reasonable agreement can be observed between the X-FEM computational models and those obtained by an adaptive finite element method. It can be concluded that while the proposed coupling X-FEM method can be used for modeling the hydraulic fracture propagation in both permeable and impermeable domains, the 'time-dependent constant pressure algorithm' can efficiently be applied as a simple computational algorithm in the framework of X-FEM formulation of deformable porous media for the case of impermeable medium.

8 Conclusion

In the present paper, the hydraulic fracture propagation was presented in saturated porous media using the extended finite element method. The mass balance equation of fluid phase and the momentum balance of bulk and fluid phases were employed to obtain the fully coupled set of equations in the framework of $u-p$ formulation. The fluid flow within the fracture was modeled using the Darcy law, in which the fracture permeability was assumed according to the cubic

Fig. 13 The contours of maximum principal stress using the coupling X-FEM method and the X-FEM method based on the 'partitioned solution algorithm'
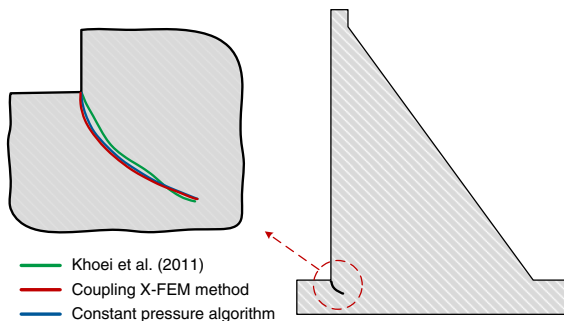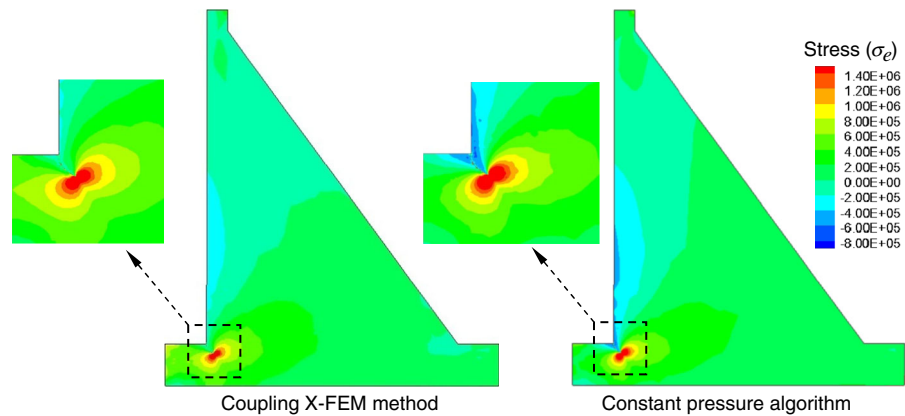

Fig. 14 The patterns of crack growth in concrete dam using the coupling X-FEM method and the 'constant pressure algorithm'

tion, the discontinuity in the displacement field was modeled using the Heaviside and crack-tip asymptotic functions, and the discontinuity in the fluid flow normal to the fracture was modeled using the modified level-set function. Two alternative computational algorithms were employed based on a 'partitioned solution algorithm' and a 'time-dependent constant pressure algorithm' to compute the interfacial forces due to fluid pressure exerted on the fracture faces in impermeable media.

Finally, several numerical examples were solved to illustrate the performance of the X-FEM method for hydraulic fracture propagation in saturated porous media. The first example was chosen to demonstrate the robustness of X-FEM in mixed mode fracture analysis of an infinite saturated porous media with an inclined crack. The last two examples were chosen to demonstrate the robustness of X-FEM technique in simulation of hydraulically driven fracture propagation in an infinite poroelastic medium and a grav-

law. The spatial discritization was performed using the extended finite element method, the time domain discritization was performed based on the generalized Newmark scheme, and the non-linear system of equations was solved using the Newton–Raphson iterative procedure. In order to perform the X-FEM formula-

Fig. 15 The variations with time of the crack length (CL) and crack mouth opening displacement (CMOD). A comparison between the coupling X-FEM method and the 'constant pressure algorithm'
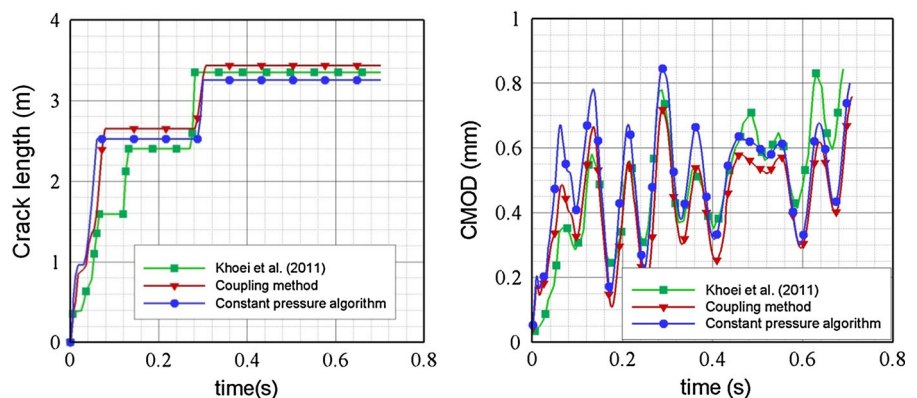
ity dam under hydrostatic pressure. It was shown that the proposed coupling X-FEM method can efficiently be used for modeling the hydraulic fracture propagation in deformable porous medium. Furthermore, it was shown that the 'time-dependent constant pressure algorithm' can be used as a simplified computational algorithm with a reasonable convergence rate in the framework of X-FEM formulation for an impermeable porous medium.

References

Akulich AV, Zvyagin AV (2008) Interaction between hydraulic and natural fractures. Fluid Dyn 43:428–435

Areias PMA, Belytschko T (2005) Analysis of three-dimensional crack initiation and propagation using the extended finite element method. Int J Numer Methods Eng 63:760–788

Barani OR, Khoei AR, Mofid M (2011) Modeling of cohesive crack growth in partially saturated porous media: a study on the permeability of cohesive fracture. Int J Fract 167:15–31

Barenblatt GI (1962) The mathematical theory of equilibrium cracks in brittle fracture. Adv Appl Mech 7:55–62

Bazant ZP, Planas J (1998) Fracture and size effect in concrete and other quasibrittle materials. CRC Press, New York

Belytschko T, Black T (1999) Elastic crack growth in finite elements with minimal remeshing. Int J Numer Methods Eng 45:601–620

Belytschko T, Moës N, Usui S, Parimi C (2001) Arbitrary discontinuities in finite elements. Int J Numer Methods Eng 50:993–1013

Belytschko T, Chen H, Xu J, Zi G (2003) Dynamic crack propagation based on loss of hyperbolicity and a new discontinuous enrichment. Int J Numer Methods Eng 58:1873–1905

Belytschko T, Gracie R, Ventura G (2009) A review of extended/generalized finite element methods for material modeling. Model Simul Mater Sci Eng 17:043001

Biot MA (1941) General theory of three dimensional consolidation. J Appl Phys 12:155–164

Biot MA, Willis PG (1957) The elastic coefficients of the theory consolidation. J Appl Mech 24:594–601

Boone TJ, Ingraffea AR (1990) A numerical procedure for simulation of hydraulically driven fracture propagation in poroelastic media. Int J Numer Anal Methods Geomech 14:27–47

Bordas S, Legay A (2005) X-FEM mini-course. EPFL, Lausanne

Bowen RM (1976) Theory of mixtures in continuum physics. Academic Press, New York

Callari C, Armero F, Abati A (2010) Strong discontinuities in partially saturated poroplastic solids. Comp Methods Appl Mech Eng 199:1513–1535

Chan AHC (1988) A unified finite element solution to static and dynamic geomechanics problems. Ph.D. dissertation, University of Wales Swansea, Wales, UK

Coussy O (2004) Poromechanics. Wiley, Chichester

Daux C, Moës N, Dolbow J, Sukumar N, Belytschko T (2000) Arbitrary branched and intersecting cracks with the extended finite element method. Int J Numer Methods Eng 48:1741–1760

De Boer R, Kowalski SJ (1983) A plasticity theory for fluid saturated porous solids. Int J Eng Sci 21:1343–1357

De Borst R, Réthoré J, Abellan MA (2006) A numerical approach for arbitrary cracks in a fluid-saturated medium. Arch Appl Mech 75:595–606

Derski W (1978) Equations of motion for a fluid-saturated porous solid. Bull Acad Polish Sci Tech 26:11–16

Detournay E (2004) Propagation regimes of fluid-driven fractures in impermeable rocks. Int J Geomech 4:35–45

Dolbow JE, Moës N, Belytschko T (2001) An extended finite element method for modeling crack growth with frictional contact. Comput Methods Appl Mech Eng 190:6825–6846

Dong CY, de Pater CJ (2001) Numerical implementation of displacement discontinuity method and its application in hydraulic fracturing. Comput Methods Appl Mech Eng 191:745–760

Dugdale DS (1960) Yielding of steel sheets containing slits. J Mech Phys Solids 8:100–108

Emerman SH, Turcotte DL, Spence DA (1986) Transport of magma and hydrothermal solutions by laminar and turbulent fluid fracture. Phys Earth Planet Inter 41:249–259

Fries TP, Belytschko T (2010) The extended/generalized finite element method: an overview of the method and its applications. Int J Numer Methods Eng 84:253–304

Geertsma J, De Klerk F (1969) A rapid method of predicting width and extent of hydraulically induced fractures. J Pet Technol 21(12):1571–1581

Ghaboussi J, Wilson EL (1972) Variational formulation of dynamics of fluid saturated porous elastic solids. J Eng Mech Div 98(EM4):947–963

Green AE, Naghdi PM (1969) On basic equations for mixtures. Q J Mech Appl Math 22(4):427–438

Jenq Y, Shah SP (1991) Features of mechanics of quasi-brittle crack propagation in concrete. Int J Fract 51:103–120

Khoei AR (2014) Extended finite element method, theory and applications. Wiley, London

Khoei AR, Haghighat E (2011) Extended finite element modeling of deformable porous media with arbitrary interfaces. Appl Math Model 35:5426–5441

Khoei AR, Karimi K (2008) An enriched-FEM model for simulation of localization phenomenon in Cosserat continuum theory. Comput Math Sci 44:733–749

Khoei AR, Nikbakht M (2007) An enriched finite element algorithm for numerical computation of contact friction problems. Int J Mech Sci 49:183–199

Khoei AR, Azami AR, Haeri SM (2004) Implementation of plasticity based models in dynamic analysis of saturated–unsaturated earth and rockfill dams. Comput Geotech 31:385–410

Khoei AR, Anahid M, Shahim K (2008a) An extended arbitrary Lagrangian–Eulerian finite element method for large deformation of solid mechanics. Finite Elem Anal Des 44:401–416

Khoei AR, Azadi H, Moslemi H (2008b) Modeling of crack propagation via an automatic adaptive mesh refinement based

on modified superconvergent patch recovery technique. Eng Fract Mech 75:2921–2945

Khoei AR, Moslemi H, Ardakany KM, Barani OR, Azadi H (2009) Modeling of cohesive crack growth using an adaptive mesh refinement via the modified-SPR technique. Int J Fract 159:21–41

Khoei AR, Barani OR, Mofid M (2011) Modeling of dynamic cohesive fracture propagation in porous saturated media. Int J Numer Anal Methods Geomech 35:1160–1184

Leung KH (1984) Earthquake response of saturated soils and liquefaction. Ph.D. dissertation, University of Wales Swansea, Wales, UK

Lewis RW, Rahman NA (1999) Finite element modeling of multiphase immiscible flow in deforming porous media for subsurface systems. Comput Geotech 24:41–63

Lewis RW, Schrefler BA (1998) The finite element method in the static and dynamic deformation and consolidation of porous media. Wiley, New York

Melenk JM, Babuska I (1996) The partition of unity finite element method: basic theory and applications. Comput Methods Appl Mech Eng 139:289–314

Moës N, Belytschko T (2002) Extended finite element method for cohesive crack growth. Eng Fract Mech 69:813–833

Moës N, Dolbow JE, Belytschko T (1999) A finite element method for crack growth without remeshing. Int J Numer Methods Eng 46:131–150

Mohammadnejad T, Khoei AR (2013a) Hydro-mechanical modeling of cohesive crack propagation in multiphase porous media using the extended finite element method. Int J Numer Anal Methods Geomech 37:1247–1279

Mohammadnejad T, Khoei AR (2013b) An extended finite element method for hydraulic fracture propagation in deformable porous media with the cohesive crack model. Finite Elem Methods Anal Des 73:77–95

Morland LW (1972) A simple constitutive theory for fluid saturated porous solids. J Geophys Res 77:890–900

Moslemi H, Khoei AR (2009) 3D adaptive finite element modeling of non-planar curved crack growth using the weighted super-convergent patch recovery method. Eng Fract Mech 76:1703–1728

Oettl G, Stark RF, Hofstetter G (2004) Numerical simulation of geotechnical problems based on a multi-phase finite element approach. Comput Geotech 31:643–664

Preisig M, Prevost JH (2011) Stabilization procedures in coupled poromechanics problem: a critical assessment. Int J Numer Anal Methods Geomech 35:1207–1225

Proceedings of 5th ICOLD international benchmark workshop on numerical analysis of dams, Denver, Colorado, 1999

Remmers JJC, de Borst R, Needleman A (2008) The simulation of dynamic crack propagation using the cohesive segments method. J Mech Phys Solids 56:70–92

Réthoré J, de Borst R, Abellan MA (2007a) A discrete model for the dynamic propagation of shear bands in a fluid-saturated medium. Int J Numer Anal Methods Geomech 31:347–370

Réthoré J, de Borst R, Abellan MA (2007b) A two-scale approach for fluid flow in fractured porous media. Int J Numer Methods Eng 71:780–800

Rice JR, Cleary MP (1976) Some basic stress diffusion solutions for fluid-saturated elastic porous media with compressible constituents. Rev Geophys Space Phys 14:227–241

Schrefler BA, Scotta R (2001) A fully coupled dynamic model for two-phase fluid flow in deformable porous media. Comput Methods Appl Mech Eng 190:3223–3246

Schrefler BA, Zhan X (1993) A fully coupled model for water-flow and airflow in deformable porous media. Water Resour Res 29(1):155–167

Schrefler BA, Zhan X, Simoni L (1995) A coupled model for water flow, airflow and heat flow in deformable porous media. Int J Heat Fluid Flow 5:531–547

Schrefler BA, Secchi S, Simoni L (2006) On adaptive refinement techniques in multi-field problems including cohesive fracture. Comput Methods Appl Mech Eng 195:444–461

Secchi S, Simoni L, Schrefler BA (2007) Mesh adaptation and transfer schemes for discrete fracture propagation in porous materials. Int J Numer Anal Methods Geomech 31:331–345

Sheng D, Sloan SW, Gens A, Smith DW (2003) Finite element formulation and algorithms for unsaturated soils. Part I: theory. Int J Numer Anal Methods Geomech 27:745–765

Shum KM, Hutchinson JW (1990) On toughening by microcracks. Mech Math 9:83–91

Simoni L, Schrefler BA (1991) A staggered finite element solution for water and gas flow in deforming porous media. Commun Appl Numer Methods 7:213–223

Spence DA, Sharp P (1985) Self-similar solutions for elasto-hydrodynamic cavity flow. Proc R Soc Lond A 400:289–313

Stelzer R, Hofstetter G (2005) Adaptive finite element analysis of multi-phase problems in geotechnics. Comput Geotech 32:458–481

Stolarska M, Chopp DL (2003) Modeling thermal fatigue cracking in integrated circuits by level sets and the extended finite element method. Int J Eng Sci 41(20):2381–2410

Sukumar N, Chopp DL, Moës N, Belytschko T (2001) Modeling holes and inclusions by level sets in the extended finite-element method. Comput Methods Appl Mech Eng 190:6183–6200

Sun WC, Ostien JT, Salinger AG (2013) A stabilized assumed deformation gradient finite element formulation for strongly coupled poromechanical simulations at finite strain. Int J Numer Anal Methods Geomech 37:2755–2788

Terzaghi K (1943) Theoretical soil mechanics. Wiley, New York

Ventura G, Budyn E, Belytschko T (2003) Vector level sets for description of propagating cracks in finite elements. Int J Numer Methods Eng 58:1571–1592

Witherspoon PA, Wang JSY, Iwai K, Gale JE (1980) Validity of cubic law for fluid flow in a deformable rock fracture. Water Resour Res 16:1016–1024

Wu YS, Forsyth PA (2001) On the selection of primary variables in numerical formulation for modeling multiphase flow in porous media. J Contam Hydrol 48:277–304

Zhang Z, Ghassemi A (2011) Simulation of hydraulic fracture propagation near a natural fracture using virtual multidimensional internal bonds. Int J Numer Anal Methods Geomech 35:480–495

Zienkiewicz OC, Shiomi T (1984) Dynamic behavior of saturated porous media: the generalized Biot formulation and it's numerical solution. Int J Numer Anal Methods Geomech 8:71–96

Zienkiewicz OC, Chan AHC, Pastor M, Paul DK, Shiomi T (1990a) Static and dynamic behavior of geomaterials—a rational approach to quantitative solutions, part I-fully saturated problems. Proc R Soc Lond A429:285–309

Zienkiewicz OC, Xie YM, Schrefler BA, Ledesma A, Bicanic N (1990b) Static and dynamic behaviour of soils: a rational approach to quantitative solutions, part 11: semisaturated problems. Proc R Soc Lond A429:310–323

Zienkiewicz OC, Chan AHC, Pastor M, Schrefler BA, Shiomi T (1999) Computational geomechanics with special reference to earthquake engineering. Wiley, New York